


2019

Determining the Precambrian Structure and Thermotectonic Evolution of the Central Ruby Range, southwest Montana

Sara Vivienne Stotter
University of Montana, Missoula

Let us know how access to this document benefits you.

Follow this and additional works at: <https://scholarworks.umt.edu/etd>

 Part of the [Geology Commons](#), and the [Tectonics and Structure Commons](#)

Recommended Citation

Stotter, Sara Vivienne, "Determining the Precambrian Structure and Thermotectonic Evolution of the Central Ruby Range, southwest Montana" (2019). *Graduate Student Theses, Dissertations, & Professional Papers*. 11417.
<https://scholarworks.umt.edu/etd/11417>

This Thesis is brought to you for free and open access by the Graduate School at ScholarWorks at University of Montana. It has been accepted for inclusion in Graduate Student Theses, Dissertations, & Professional Papers by an authorized administrator of ScholarWorks at University of Montana. For more information, please contact scholarworks@mso.umt.edu.

DETERMINING THE PRECAMBRIAN STRUCTURE AND THERMOTECTONIC EVOLUTION
OF THE CENTRAL RUBY RANGE, SOUTHWEST MONTANA

By

Sara Vivienne Stotter

B.S. Geology, Bucknell University, Lewisburg, Pennsylvania, 2016

Thesis

Presented in partial fulfillment of the requirements
for the degree of

Master of Science
in Geosciences

Spring 2019

Approved by:

Scott Whittenburg, Dean of the Graduate School
Graduate School

Julia Baldwin, Committee Chair
Geosciences

James Sears, Committee Co-Chair
Geosciences

Kent Sugden, Committee Co-Chair
Chemistry and Biochemistry

Determining the Precambrian structure and thermotectonic evolution of the central Ruby Range, southwest Montana

Chairperson: Dr. Julia Baldwin

The Ruby Range in southwestern Montana is a fundamental location within the Archean Wyoming craton for examining Precambrian crustal architecture and determining the thermotectonic evolution of the region. Monazite, zircon, and garnet geochronology from each of the three major units within the Ruby Range reveal two distinct metamorphic age populations: an older population ca. 2.55-2.45 Ga (the Tendoy orogeny) and a second, younger population ca. 1.78-1.72 Ga (the Big Sky orogeny). Phase equilibria modeling for the Big Sky orogeny within the confines of the Mine Gulch 7.5' quadrangle reveal discrete pressure-temperature (P - T) histories for each of the three major structural units within the range. The Christensen Ranch metasedimentary suite yields peak metamorphic pressures of ~ 7 kbar, however peak temperatures increase from the top of the unit towards the base from ~ 700 °C to ~ 760 °C. The Dillon Gneiss yielded peak metamorphic conditions of ~ 8.4 kbar and ~ 760 °C, and the Elk Gulch Suite on average yielded peak conditions of ~ 8.8 kbar and ~ 770 °C. Additionally, new mapping interpretations from the Mine Gulch quadrangle reveal that all three units within the Ruby Range are closely structurally related, sharing an entwined Precambrian metamorphic and deformational history. Furthermore, the separation of the ca. 2.45 Ga garnet leucogneiss from the Dillon Gneiss as a distinct unit within the range ascribes wide spread crustal melting to the Tendoy orogeny. Combining these new observations with previous work aid in constraining a revised tectonic history for southwestern Montana between ~ 2.55 -1.72 Ga. Prior to ~ 2.55 Ga, sediment accumulated on the margin of the Wyoming province and was followed by continental collision, the Tendoy orogeny, between ~ 2.55 -2.45 Ga. A second cycle of sedimentation on the cratonic margin initiated immediately after the conclusion of the Tendoy orogeny and lasted between ~ 2.45 -1.8 Ga. Between ~ 2.1 -2.0 Ga, the Wyoming Province experienced a short period of extensional tectonism resulting in the emplacement of mafic dikes and sills. Between ~ 1.9 -1.8 Ga, the Wyoming Province began to subduct beneath the Medicine Hat Block, ultimately culminating in the collision between the two continents resulting in the Big Sky orogeny between ~ 1.78 -1.72 Ga.

Acknowledgements

I would like to express my sincere gratitude to everyone who made this project possible. Foremost, I would like to thank my advisor Dr. Julia Baldwin for your guidance and unwavering support. I am incredibly appreciative of how patient you were with me, and for never once turning me away from your door when I came by with countless questions. I've truly had an amazing time working with you these past three years. I would also like to thank our collaborator Dr. Tekla Harms for your additional support and for sharing your immense wealth of knowledge with me. Thanks to Jesse Mosolf, Paul Thale, and Susan Smith from the Montana Bureau of Mines and Geology for helping me with GIS and for helping me construct my map. I would also like to thank my other committee members Dr. James Sears and Dr. Kent Sugden for their time and feedback throughout this process. Finally, I would like to thank my mom and brother for endlessly supporting me throughout my time in Montana. This research was supported by funds from the USGS EDMAP Program, the Geological Society of America, the Wyoming Geological Association, and Indiana University.

TABLE OF CONTENTS

Abstract	ii
Acknowledgements	iii
Table of Contents	iv
List of Figures	vi
List of Tables	vii
1. Introduction	1
2. Geologic Setting	3
2.1. Regional geology	3
2.2. Ruby Range	7
3. Field relationships	13
4. Methods	18
4.1. Field work and mapping	18
4.2. Petrography	19
4.3. Bulk rock chemistry	20
4.4. Mineral chemistry	20
4.5. Thermodynamic modeling	23
5. Mapping results	24
6. Petrography	26
6.1. Sample 17-SS-8	28
6.2. Sample 14-CH-9a	31
6.3. Sample 17-SS-17	32
6.4. Sample SC13-7	34
6.5. Sample SW13-2	36
6.6. Sample 14-RG-01b	38
7. Mineral chemistry	40
7.1. Sample 17-SS-8	42
7.2. Sample 14-CH-9a	42
7.3. Sample 17-SS-17	42
7.4. Sample SC13-7	45
7.5. Sample SW13-2	46

7.6. Sample 14-RG-01b	46
8. Phase equilibria modeling	47
8.1. Sample 17-SS-8	47
8.2. Sample 14-CH-9a	50
8.3. Sample 17-SS-17	52
8.4. Sample SC13-7	54
8.5. Sample SW13-2	56
8.6. Sample 14-RG-01b	58
9. Discussion	60
9.1. <i>P-T paths</i>	60
9.2. <i>P-T-t paths</i>	64
9.3. Implications for melt and lack of K-feldspar	66
10. Tectonic interpretation	68
10.1. Early Proterozoic collisional orogenesis: the Tendoy orogeny	68
10.2. Post 2.45 Ga extensional tectonism and dike/sill emplacement	70
10.3. Post-extensional passive margin sedimentation and the 1.78-1.72 Ga Big Sky orogeny	70
11. Conclusions	73
12. References	75

List of Figures

Figure 1: Map of Archean provinces	2
Figure 2: Precambrian uplifts of SW Montana	6
Figure 3: Simplified geologic map of Ruby Range	9
Figure 4: Photographs of select lithologies from Christensen Ranch metasedimentary suite	14
Figure 5: Photographs of quartzofeldspathic gneiss from Dillon Gneiss	16
Figure 6: Photographs of select lithologies from Elk Gulch Suite	17
Figure 7: Garnet zoning and mineral compositions	22
Figure 8: Photographs of the garnet leucogneiss	25
Figure 9: Stereonets	26
Figure 10: Sample locations	29
Figure 11: Petrography for sample 17-SS-8	30
Figure 12: Petrography for sample 14-CH-9a	33
Figure 13: Petrography for sample 17-SS-17	35
Figure 14: Petrography for sample SC13-7	37
Figure 15: Petrography for sample SW13-2	39
Figure 16: Petrography for sample 14-RG-01b	41
Figure 17: Pseudosections for sample 17-SS-8	49
Figure 18: Pseudosections for sample 14-CH-9a	51
Figure 19: Pseudosections for sample 17-SS-17	53
Figure 20: Pseudosections for sample SC13-7	55
Figure 21: Pseudosections for sample SW13-2	57
Figure 22: Pseudosections for sample 14-RG-01b	59
Figure 23: Tectonic interpretation	71

List of Tables

Table 1: Previously reported geochronology	11
Table 2: Previously reported <i>P-T</i> work	12
Table 3: Unnormalized bulk rock chemistry	21
Table 4: Normalized bulk rock chemistry for THERMOCALC	21
Table 5: Sample locations and mineralogy	27
Table 6: Representative garnet SEM-EDS analyses	43
Table 7: Representative biotite SEM-EDS analyses	44
Table 8: Representative plagioclase SEM-EDS analyses	45
Table 9: Representative cordierite SEM-EDS analyses	47

1. Introduction

Deciphering the Precambrian thermotectonic evolution of the Wyoming craton is crucial to understanding the crustal assembly and modification of Laurentia. A key location for examining this Precambrian crustal architecture is the Ruby Range, one of several basement-cored Laramide uplifts located on the northwestern margin of the Wyoming craton in southwestern Montana (Figure 1). The Ruby Range is located within the Montana Metasedimentary Terrane (MMT), which is distinguished from surrounding terranes by the presence of distinctive metasupracrustal sequences and intercalated volcanics within a variety of volumetrically abundant quartzofeldspathic gneisses (Mogk et al., 1992). A metasedimentary sequence comprised of thick marble packages suggestive of passive margin sediments occurs along the western flank of the range. This feature suggests that rocks in this region have likely preserved the geologic record of regionalized tectonic processes at the cratonic margin during the Proterozoic. Examining the late Archean to Proterozoic evolution of the Ruby Range will not only elucidate the tectonic history of the MMT, but will also aid in revealing how continents form, how they grow, and how they stabilize through time.

This study integrates the mapping of the Mine Gulch 7.5' quadrangle with petrological analysis and pressure-temperature ($P-T$) phase equilibria modeling to place quantitative constraints on the Proterozoic metamorphic and tectonic evolution of rocks in the central portion of the Ruby Range. Originally, it was assumed that all rocks within the Wyoming Province were Archean in age, however Giletti (1966) determined that the basement rocks of southwestern Montana experienced a regional ~ 1.6 Ga thermal resetting event based on isotopic K-Ar and Rb-Sr ages. More recent work has expanded on this precedent, revealing that Precambrian basement in southwestern Montana experienced profound thermal reworking at both ca. 2.45 Ga and during the 1.78 Ga Big Sky orogeny

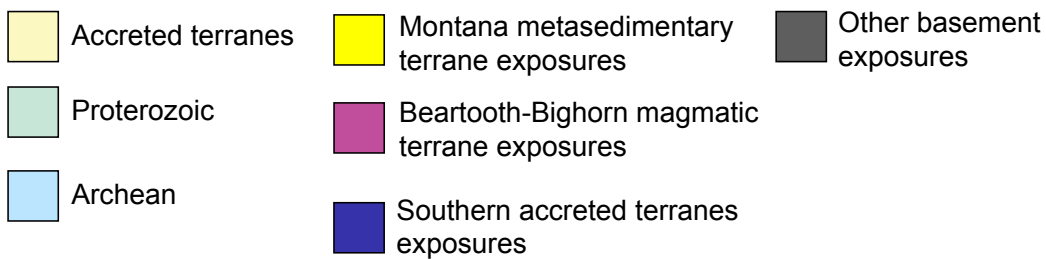
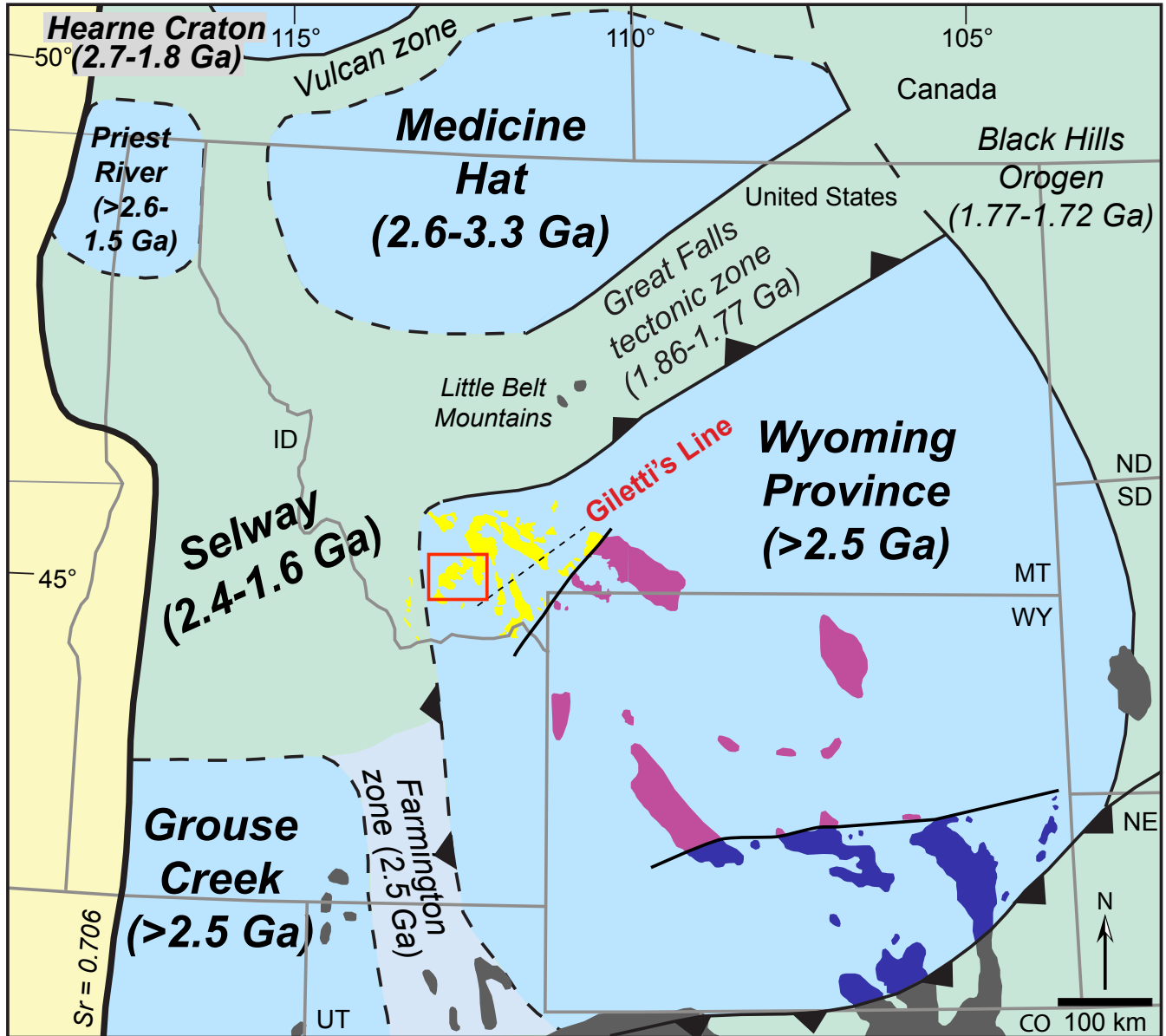


Figure 1. Simplified map of Archean basement provinces of southwest Laurentia with Wyoming province basement exposures colored by terrane. The study area, the Ruby Range, is bounded by the red box Modified after Foster et al. (2006) and Muller and Frost (2006).

(Roberts et al., 2002; Kellogg et al., 2003; Harms et al., 2004; Brady, et al., 2004; Cheney et al., 2004; Jones, 2008; Cramer, 2015). Mapping and evaluating the structural relationships of the major units within the Ruby Range on the 7.5' quadrangle scale will allow for an improved understanding of the more generalized crustal architecture of the MMT during these two crucial times in the Precambrian history of the Wyoming craton. Combining these new interpretations with petrologic observations of peak mineral assemblages alongside associated *P-T* constrains revealed will further elucidate the nature of both Paleoproterozoic thermotectonic events. Ultimately, studying cratonic margins such as this will aid in a better understanding of how Earth's crust has changed in the past and will allow us to compare ancient tectonic processes to modern ones.

2. Geologic Setting

2.1. Regional geology

The Wyoming Province is an Archean craton that underlies parts of Montana and Wyoming, and is considered to be part of the initial core of the North American continent (Figure 1). It is one of seven provinces that comprise North America (or Laurentia), in addition to the Hearne, Rae, Slave, Nain, Superior, and Burwell Provinces. U-Pb detrital zircon ages from the Beartooth Mountains, the Tobacco Root Mountains, and the Ruby Range indicate that the Wyoming Province formed during a period of significant crustal growth between 3.4 and 3.2 Ga (Mueller et al., 1998). The Wyoming Province can be subdivided into three geologically distinct terranes: the Beartooth-Bighorn Magmatic Terrane (BBMT), the Southern Accreted Terranes (SAT), and the Montana Metasedimentary Terrane (MMT). The BBMT is dominated by the presence of 3.0-2.8 Ga tonalitic-trondhjemitic-granodioritic metaplutonic rocks, in addition to lesser amounts of high-K granites and granodiorites (Mogk et al., 1992; Mueller and Frost, 2006; Frost et al., 2006). The SAT is characterized by magmatic and tectonic activity (ca. 2.67-2.68 Ga

and ca. 2.72 Ga) which is slightly younger than that of the BBMT (ca. 2.75-2.95) (Chamberlain et al., 2003; Mueller and Frost, 2006; Frost et al., 2006). These terranes are comprised of sequences of felsic, mafic, and ultramafic volcanics, in addition to metasedimentary rocks including pelitic schist, quartzite, and iron formation thought to have formed during Late Archean calc-alkalic magmatism and tectonism, most likely representing a period of crustal growth (Mueller and Frost, 2006). The MMT, the terrane in which the Ruby Range is located, is comprised of younger, Late Archean quartzite, pelite, and carbonate rock associations intercalated with older Archean ca. 3.2-3.0 Ga quartzofeldspathic gneisses in which belts of metasupracrustal sequences are preserved (Mogk et al., 1992; Mueller et al., 1993, 2004; Mueller and Frost, 2006).

The aerial extent of the Wyoming Province is defined by three Proterozoic collisional orogens: the Black Hills Orogen to the east, the Cheyenne Belt to the south, and the Great Falls Tectonic Zone (GFTZ) to the northwest (Harms et al., 2004; Brady, et al., 2004; Mueller et al., 2005; Mueller and Frost, 2006) (Figure 1). The Black Hills Orogen represents the collision of the Wyoming Province with the Superior Province between 1.77-1.71 Ga, not to be confused with the older, 1.86-1.79 Ga Trans-Hudson orogen (Hearne-Superior convergence) to the north (Dahl et al., 1999). The Cheyenne Belt, located on the southern margin of the Wyoming Province, is the tectonic suture zone which records the collision between the Wyoming Craton and Paleoproterozoic Yavapai Province between 1.78-1.72 Ga (Chamberlain, 1998; Whitmeyer and Karlstrom, 2007). The northwestern margin of the Wyoming Province, the GFTZ, has thus been interpreted as recording ocean basin closure followed by collision between the Wyoming Province and Medicine Hat Block, another Archean terrane, between 1.78-1.72 Ga.

Giletti (1966) first assessed the timing and nature of metamorphism within the MMT along the northwestern margin of the Wyoming Province. Prior to Giletti's work, it was inferred that all rocks in

the Wyoming Province were Archean in age. Based on K-Ar and Rb-Sr ages, Giletti (1966) reasoned that the basement rocks of southwest Montana experienced a regional 1.6 Ga thermal resetting event. In contrast, rocks immediately to the southeast of this zone yielded older K-Ar and Rb-Sr ages between 3.2-2.1 Ga, indicating that rocks in this area have not been thermally reset by a regional metamorphic event (Giletti, 1966). This boundary of isotopic resetting has since become known as ‘Giletti’s Line’ (Giletti, 1966) (Figure 2). Later, James and Hodge (1980) confirmed Giletti’s regional 1.6 Ga thermal resetting event, and ascribed regional metamorphism and deformation to a 2.75 Ga orogeny.

The GFTZ is located to the northwest of Giletti’s Line, and is a broad zone of northeast trending, high-angle thrust faults that extends from northeastern Idaho to southern Canada (Harms et al., 2004; Burger, et al., 2004; Gifford et al., 2014). For some time, the origin of the GFTZ has been up to debate due to lack of exposure. The only surficial expression of the GFTZ is found in the Little Belt Mountains, where rocks are dominated by 1.86 Ga calc-alkaline intrusives (Foster et al., 2007). The rocks of the Little Belt Mountains have also been found to exhibit a geochemical character consistent with such observed at subduction zones, which supports the idea that the GFTZ marks the suture zone between the Wyoming Province and Medicine Hat Block (Mueller et al., 2002; Vogl et al., 2004). This collisional tectonothermal event has been termed the Big Sky orogeny, and has been best documented within the Tobacco Root Mountains which lies approximately 40 km to the northwest of the Ruby Range (Harms et al., 2004). Architecturally, the Ruby Range, Tobacco Root Mountains, the Highland Mountains, and the northern part of the Gravelly Range all comprise the metamorphic core of the orogen (Harms et al., 2004).

The Big Sky orogeny has been characterized as an upper amphibolite to lower granulite facies metamorphic event which occurred between 1.78-1.72 Ga, with a clockwise *P-T* path recording peak

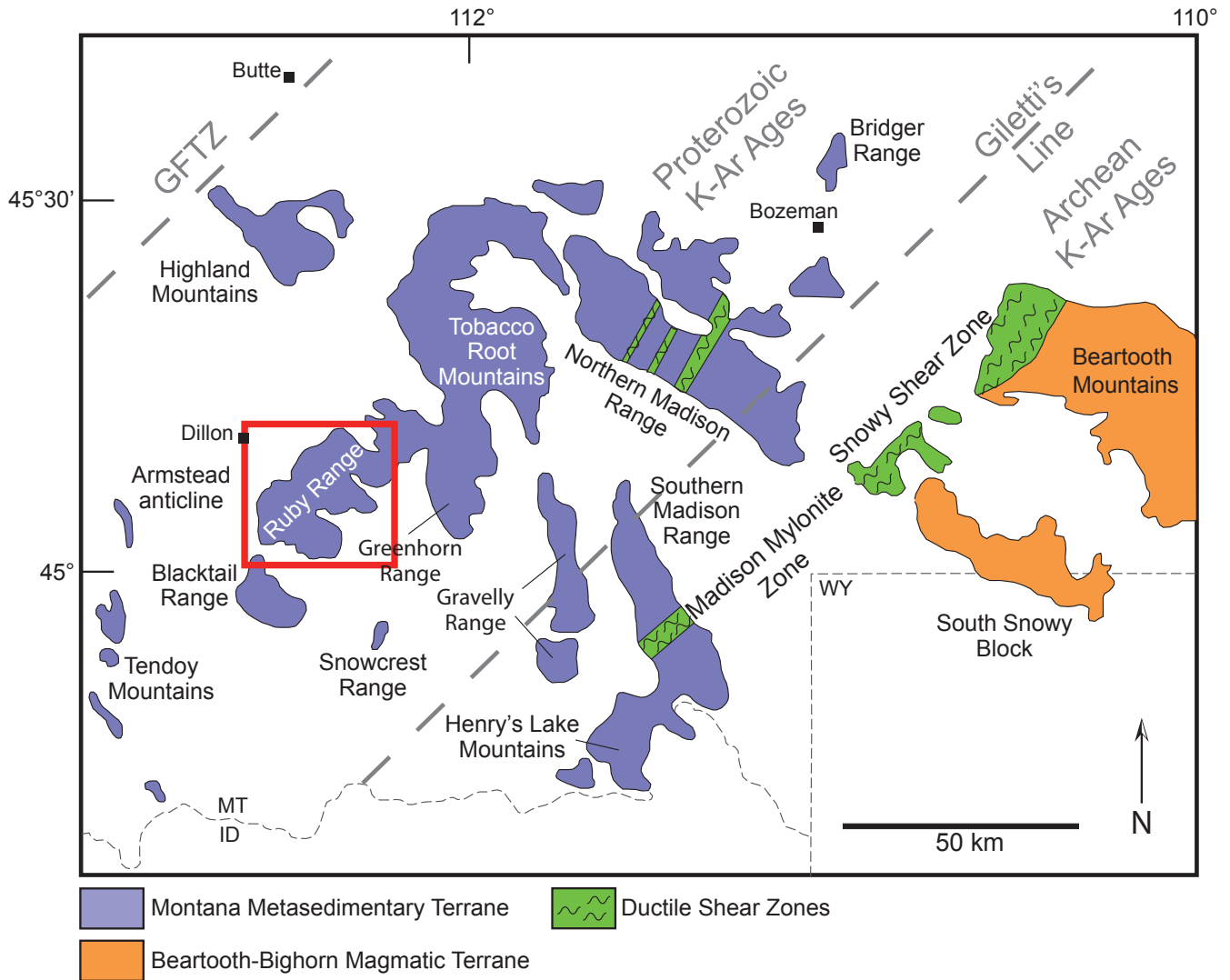


Figure 2. Map of southwest Montana exhibiting location of basement exposures colored by terrane and position of Gilletti's Line. The study area, the Ruby Range, is bounded by a red box. Modified from Mogk et al. (1992).

metamorphic conditions of >10 kbar and $700-800$ °C (Cheney et al., 2004). During subsequent unroofing, rocks experienced near isothermal decompression to 5 kbar. Within the Tobacco Root Mountains, the Spuhler Peak Metamorphic Suite is the only suite of rocks that strictly exhibits Proterozoic ages of 1.78-1.72 Ga, which is predominantly comprised of allochthonous mafic volcanics and sediments that were deposited in a marine environment and subsequently accreted during the Big Sky orogeny (Harms et al., 2004).

A pre-Big Sky orogeny tectonothermal event has additionally been identified throughout the MMT. Kellogg et al. (2003) conducted U-Pb TIMS analyses on zircons from a series of high-grade felsic gneisses in the Tendoy and Beaverhead Mountains of southwestern Montana which are located approximately 50 miles south of the Ruby Range. The study yielded Paleoproterozoic ages of 2.45 Ga from three separate localities in the region, which have been interpreted to represent the age of granitic plutonism, metamorphism, and crustal consolidation in southwest Montana (Kellogg et al., 2003). Similar 2.45 Ga ages have also been observed in garnet and monazite from a quartz-feldspar-biotite gneiss in the Tobacco Root Mountains to the north of the Ruby Range (Dahl et al., 2002; Roberts et al., 2002b). Similar 2.45 Ga ages were subsequently identified within in two major units from the Ruby Range by Jones (2008) as evidenced by metamorphic overgrowths of monazite in addition to zircon cores. The identification of 2.45 Ga ages in the Ruby Range in addition to several adjacent Laramide uplifts in southwestern Montana suggest that the Paleoproterozoic metamorphism of the MMT was widespread (Jones, 2008).

2.2. Ruby Range

The Ruby Range is located along the northwestern margin of the Wyoming Province, and is one of several metamorphic blocks that was uplifted during the Laramide orogeny. William Heinrich and J.C. Rabbitt were the first to conduct an in-depth study of the geology of the Ruby Range in the late 1940's and 1950's. These workers determined that the Ruby Range is comprised of lesser amounts of diabase dikes, peridotite intrusives, aplites, pegmatites, and quartz veins, and is dominated by three primary suites. These units were subsequently named the pre-Cherry Creek rocks, the Cherry Creek Group, and the Dillon Granite Gneiss (Heinrich, 1960). Garihan (1973) also used these three unit subdivisions for his mapping work in the Ruby Range during the 1970's and early 1980's. In the 1990's,

Harold James proposed a new nomenclature based on new stratigraphic interpretations. He termed the units, from youngest to oldest, the Christensen Ranch Metasedimentary Suite (CRMS), the Dillon quartzofeldspathic gneiss (DQFG), and the older gneiss and schist (OGS). For this study, we will also be using the CRMS, however we have decided to rename the DQFG the Dillon Gneiss (DG) and the OGS the Elk Gulch Suite (EGS) based on its type locality identified within the Ruby Range (Figure 3).

The CRMS is a complex sequence of metasedimentary and intercalated volcanic rock that occurs along the western flank of the Ruby Range. The sequence includes an abundance of calcitic and dolomitic marbles, calc-silicate, amphibolite, quartzite, pelitic schist and gneiss, garnet leucogneiss, and mylonitic garnet leucogneiss, in addition to minor amounts of metaconglomerate, anthophyllite-gedrite rocks, and banded iron formation. The Dillon Gneiss comprises the spine of the range, and is dominated by quartzofeldspathic gneiss, granitic gneiss, pelitic gneiss, amphibolite, lesser amounts of both garnet leucogneiss and mylonitic garnet leucogneiss, and minor dolomitic and calcitic marble. The protolith of the Dillon Gneiss is ambiguous in nature, and the unit has been interpreted as having both sedimentary and igneous origins (Jones, 2008). The EGS is the structurally deepest unit within the range, and is primarily composed of biotite gneiss, augen gneiss, pelitic gneiss, migmatite, hornblende gneiss, amphibolite and minor gedrite gneisses. The lack of marble and iron formation within the EGS is a defining characteristic of the unit that distinguishes it from the CRMS. Additionally, pods of meta-ultramafic rocks, ranging from ~1 m to hundreds of meters in length are present throughout all of the basement units in the Ruby Range (Desmarais, 1981).

Metamorphism in the Ruby Range was first believed to have occurred at 2.75 Ga based on Rb-Sr whole-rock dating from a suite of quartzofeldspathic gneisses (James and Hedge, 1980). Ten years later, James (1990) proposed two separate periods of metamorphism, an upper amphibolite facies event at

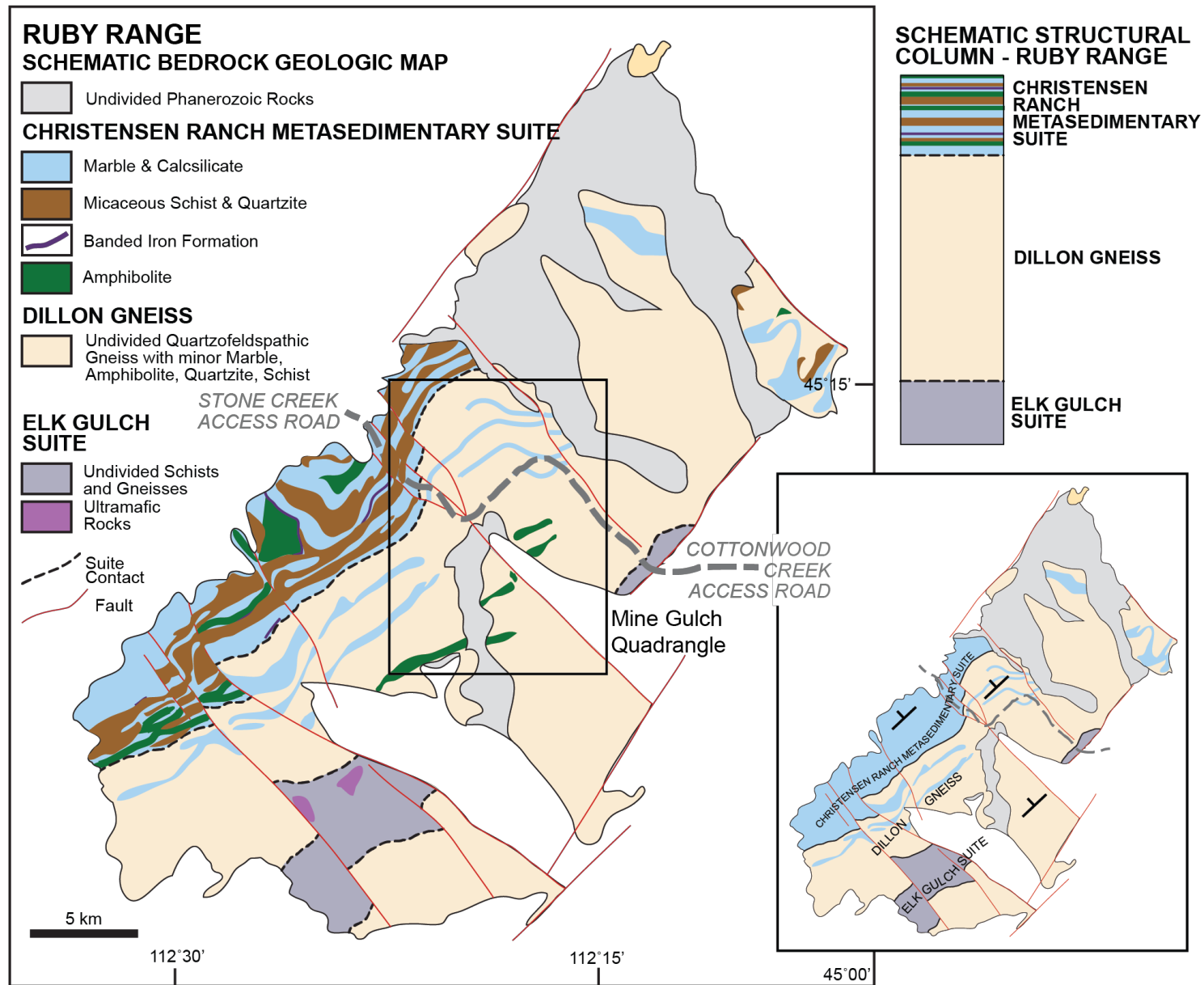


Figure 3. Simplified schematic diagram of the Ruby Range showing the divisions between the Christensen Ranch Metasedimentary Suite, the Dillon Gneiss, and the Elk Gulch Suite. Black box outlines the location of the Mine Gulch 7.5' quadrangle.

2.75 Ga and a second 1.65 Ga event related to retrograde metamorphism associated with regional thermal resetting as first proposed by Giletti (Giletti, 1966; James, 1990b).

More recently, monazite and zircon geochronology have identified three distinct age populations within the Ruby Range which includes an igneous population at 2.77 Ga and two metamorphic populations at 2.45 Ga and 1.78 Ga (Roberts et al., 2002; Dahl et al., 2002; Kellogg et al., 2003; Harms et al., 2004; Brady, et al., 2004; Jones, 2008; Mueller et al., 2012; Alcock et al., 2013) (Table 1). The 2.77 Ga event represents the intrusive age of the Dillon Gneiss (DG) based on isotopic dating (Jones, 2008). Jones additionally proposed two possible protoliths for the DG: either the DG was formed from arkosic sediments derived from the Beartooth arc terrane, or that the DG originated as a volcanic ash deposit associated with the 2.78 Ga Beartooth arc (Jones, 2008). Two metamorphic age populations were further supported by work conducted by Cramer (2015), which confirmed that monazite grew during two distinct phases between 1.79-1.72 Ga and 2.52-2.45 Ga. The 2.45 Ga and 1.78 Ga ages, respectively, correspond to the aforementioned cryptic 2.45 Ga crustal melting and metamorphic event and Big Sky orogeny which affected the entirety of the MMT.

Dahl (1979, 1980) was the first to determine *P-T* constraints for peak metamorphic conditions in the Ruby Range from two localities; Kelly Creek situated in the northwestern corner of the range and Carter Creek located along the western flank. The study utilized garnet-pyroxene geothermometry on a series of amphibolites, mafic granulites, metapelites, dolomitic marbles, and metamorphosed iron formation, and yielded peak *P-T* conditions of 724 ± 50 °C and 7.2 ± 1.2 kbar from the Kelly Creek locality and 675 ± 45 °C and 6.2 ± 1.2 from the Carter Creek locality (Dahl, 1980). A few years later, Desmarais (1981) conducted additional *P-T* work on ultramafic rocks from the range and yielded similar conditions of 710 °C and 5-7 kbar. In 2015, Hamelin conducted *P-T* work from a transect of metapelites within the CRMS, and estimated peak metamorphic temperatures during the Big Sky orogeny to be

Table 1.

Summary of previously reported ages of Ruby Range monazite and zircon geochronology. EMPA and LA-ICPMS ages are reported with 2σ errors, whereas SHRIMP ages are 1σ errors.

Unit	Rock Type	Mineral Dated	Big Sky orogeny (Ma)	Tendoy orogeny (Ma)	Igneous age (Ma)	Dating Method	Reference
CRMS	metapelitic schist	monazite	1779 ± 10			EMPA U-Th-Pb	Jones (2008)
CRMS	metapelitic schist	monazite	1814 ± 15			EMPA U-Th-Pb	Jones (2008)
CRMS	orthoamphibolite	monazite	1747 ± 6			LASS ICP-MS	Cramer (2015)
CRMS	metapelitic gneiss	monazite	1764 ± 6			LASS ICP-MS	Cramer (2015)
DG	migmatitic gneiss	zircon	1781 ± 7	2471 ± 20	2772 ± 7	SHRIMP $^{207}\text{Pb}/^{206}\text{Pb}$	Jones (2008)
DG	migmatitic gneiss	zircon			2772 ± 11	SHRIMP $^{207}\text{Pb}/^{206}\text{Pb}$	Jones (2008)
DG	migmatitic gneiss	monazite	1784 ± 54	2468 ± 11		SHRIMP $^{207}\text{Pb}/^{206}\text{Pb}$	Jones (2008)
DG	migmatitic gneiss	monazite		2404 ± 21		EMPA U-Th-Pb	Jones (2008)
DG	migmatitic gneiss	monazite		2444 ± 21		EMPA U-Th-Pb	Jones (2008)
EGS	quartzofeldspathic gneiss	zircon		2523 ± 14	2762 ± 37	SHRIMP $^{207}\text{Pb}/^{206}\text{Pb}$	Jones (2008)
EGS	quartzofeldspathic gneiss	zircon		2437 ± 47		SHRIMP $^{207}\text{Pb}/^{206}\text{Pb}$	Jones (2008)
EGS	migmatitic gneiss	monazite	1769 ± 11			LASS ICP-MS	Cramer (2015)
EGS	orthoamphibolite	monazite	1758 ± 4			LASS ICP-MS	Cramer (2015)
EGS	metapelitic gneiss	monazite	1748 ± 3	2471 ± 13		LASS ICP-MS	Cramer (2015)
EGS	metapelitic gneiss	monazite	1753 ± 6	2489 ± 8		LASS ICP-MS	Cramer (2015)
EGS	metapelitic gneiss	monazite	1752 ± 6	2480 ± 7		LASS ICP-MS	Cramer (2015)

Table 2.

Summary of previous *P-T* work completed by Hamelin (2015) and Cramer (2015).

Sample	Rock Type	Peak Mineral Assemblage (+qtz)	Peak <i>P-T</i> Conditions	Reference
14-CH-1	grt-bt-sill schist	grt + bt + sill + plag + ksp + melt	~780 °C, ~9 kbar	Hamelin (2015)
14-CH-4	grt-bt-sill schist	grt + bt + sill + plag + ilm + melt	~700 °C, ~6.8 kbar	Hamelin (2015)
14-CH-5a	grt-bt-sill schist	grt + bt + sill + plg + H ₂ O + melt	~700 °C, ~6.4 kbar	Hamelin (2015)
14-CH-9b	grt-bt-sill schist	grt + bt + sill + plag + ksp + ilm + melt	~775 °C, ~8.6 kbar	Hamelin (2015)
14-CH-11a	grt-bt-sill schist	grt + bt + sil + plag + ksp + ilm + melt	~780 °C, ~9.1 kbar	Hamelin (2015)
SC13-6	grt-sill gneiss	grt + bt + sill + plag + ksp + ilm + melt	740-770 °C, 5.7-8.5 kbar	Cramer (2015)
EG13-4	migmatitic gneiss	grt + bt + sil + plag + ksp + ilm + ru + melt	770-800 °C, 8.1-9.6 kbar	Cramer (2015)
EG13-5	grt-ged-crd gneiss	grt + bt + ged + ilm + rt	710-770 °C, 8-11 kbar	Cramer (2015)
SW13-4	grt-sil-crd gneiss	grt + bt + sil + plag + ilm + ru + melt	725-830 °C, 7.7-9.6 kbar	Cramer (2015)

~800 °C and ~9 kbar followed by subsequent decompression and cooling (Hamelin, 2015) (Table 2). The most recent *P-T* work was carried out by Cramer (2015) (Table 2) who examined three specific localities: the Stone Creek locality to the northwest of the quadrangle, the Elk Gulch locality to the south, and the Sweetwater Creek locality to the southeast (Cramer, 2015). At the Stone Creek locality, peak *P-T* conditions during the Big Sky orogeny were estimated to be ~6.5 kbar and 760 °C followed by slight decompression and cooling to ~6 kbar and 680 °C. Both the Sweetwater Creek and Elk Gulch localities were interpreted to have reached peak metamorphic conditions of ~9 kbar and 780 °C.

3. Field relationships

This study focuses on the three primary units found within the Mine Gulch quadrangle: the CRMS, the DG, and the EGS.

The CRMS is the structurally highest of the three primary units within the Ruby Range. The CRMS lies along the western flank of the range, and is present in the northwestern corner of the Mine Gulch quadrangle (Figure 3). The suite is dominated by quartzite, dolomitic and calcitic marble, amphibolite, and undifferentiated metapelitic rocks. Minor lithologies include calc-silicate gneiss, garnet leucogneiss, mylonitic garnet leucogneiss, gedrite-anthophyllite schist, metamorphosed iron formation, meta-ultramafic rocks, and pegmatite (Figure 4). Thicknesses of individual beds vary from only a few centimeters up to several hundreds of meters thick, with an estimated total thickness of ~2,000 meters (James, 1990b). In the study area, the fabric of the CRMS is predominantly NE-striking with moderate to steep NW-dipping foliation expressed as both lithologic layering in addition to isoclinal fold axes.

The DG comprises the core of the Ruby Range and is the most prevalent unit within the region by volume. It lies below the CRMS, however it is structurally concordant with all adjoining rock units in

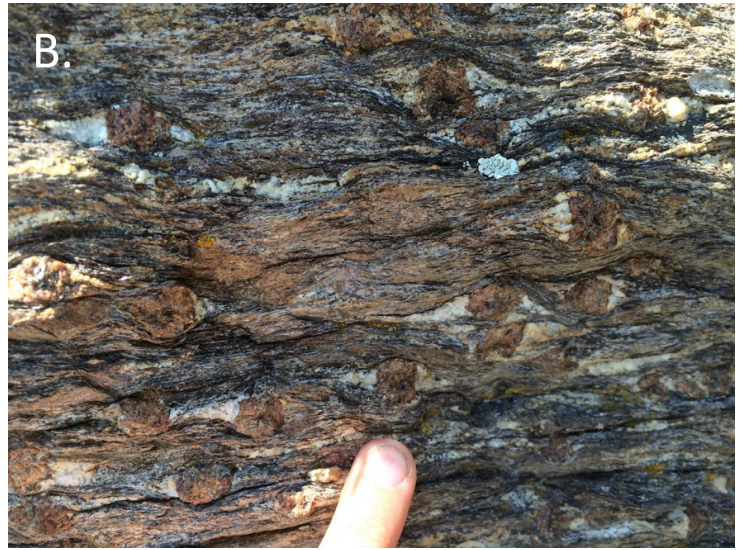


Figure 4. Field photographs of selected lithologies from the Christensen Ranch Metasedimentary Suite. **A)** Photograph of marble outcrop. **B)** Photograph of pelitic gneiss. **C)** Photograph of amphibolite gneiss. **D)** Photograph of quartzite.

the region (James, 1990b). The dominant lithology within the DG is massive to well-foliated, medium to coarse-grained, white to gray quartzofeldspathic gneiss, however many variations of this characteristic rock type have been observed (Figure 5). In places, the DG appears to be more granitic in composition with greater abundance of K-feldspar which gives the rock a characteristically reddish-brown color. Additionally, the DG often grades into a more strongly banded gneiss with a greater abundance of darker minerals including biotite, garnet, and occasionally hornblende. Within these primary lithologies, separate bodies of amphibolite and narrow ribbons of infolded marble are abundantly present, in addition to pods of meta-ultramafic material and pelitic gneisses. The fabric of the DG within the Mine Gulch Quadrangle is indistinguishable from that of the CRMS: NE-striking with moderate to steep NW-dipping foliation. The unit also contains northeast trending, shallowly dipping regional lineations.

In the Ruby Range, the EGS is the most volumetrically minor unit as well as the structurally lowest of the three main suites. The suite primarily crops out within the south-central portion of the range, but also occurs less abundantly on the eastern flank of the range, east of the map area (James, 1990b). While the EGS is generally similar in lithology throughout the Ruby Range, minor variations can be observed at different localities in the region (Figure 6), which are as follows: the Elk Gulch locality in the southern portion of the Ruby Range, the Sweetwater and Cottonwood Creek localities to the south and east of the Mine Gulch quadrangle, respectively, and the region of the EGS in the southwestern portion of the Mine gulch quadrangle. In the Elk Gulch area, the locality after which the suite has been renamed, the unit is comprised of garnet-sillimanite bearing migmatitic gneiss, garnet bearing granitic gneiss, minor garnet amphibolite, garnet-gedrite gneiss, and meta-ultramafic rock (Cramer, 2015). Fabric in this region is dominated by a NE-striking and moderately NW-dipping foliation expressed as lithologic layering and through the orientation of fold axes (Cramer, 2015). Additionally, lineations in the Elk Gulch locality are N trending with a moderate plunge. In the

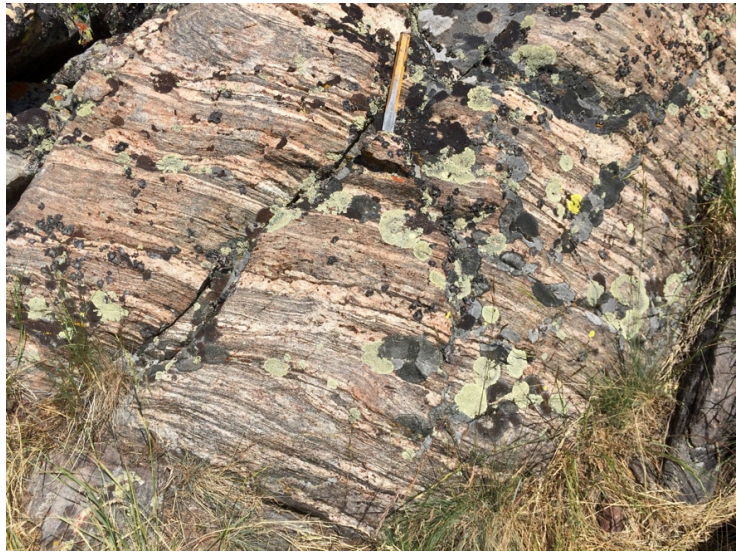


Figure 5. Field photographs of different varieties of quartzofeldspathic gneiss from the Dillon Gneiss. The variation in pink coloration correlates to the proportion of K-feldspar present in the outcrop.



Figure 6. Field photographs of various outcrops from the EGS located in the southwestern corner of the map area. In this region, the EGS is comprised primarily of garnet-sillimanite migmatitic gneiss, garnet bearing granitic gneiss, amphibolite and garnet amphibolite, and meta-ultramafic rock.

Sweetwater and Cottonwood Creek areas, the unit is also comprised of garnet amphibolite and meta-ultramafic rock, but differences arise based on the presence of garnet-bearing migmatitic gneiss, granitic gneiss, garnetiferous quartzofeldspathic gneiss, garnet-sillimanite \pm cordierite gneiss, and garnet leucogneiss (Cramer, 2015). The fabric of these areas are generally dominated by a NE-striking and moderate to steeply dipping SE foliation, also expressed as lithologic layering and through the orientation of fold axes (Cramer, 2015). Lineations are primarily NE trending with a shallow plunge. The EGS in the southwestern corner is more similar to the Elk Gulch locality than the Sweetwater and Cottonwood Creek localities, but does not contain garnet-gedrite gneiss and has greater quantities of amphibolite. In this area the foliation is primarily NE-striking and dips steeply to the NW, with lineations that trend towards the NE with moderate plunges (James, 1990a).

4. Methods

4.1. Field work and mapping

Mapping of the 1:24,000 Mine Gulch USGS 7.5' quadrangle was completed during the summer of 2017. The mapping of the quadrangle is part of a collaborative effort between the Montana Bureau of Mines and Geology and the United States Geological Survey's EDMAP program. In accordance with this program, the finished map will be published by the Montana Bureau of Mines and Geology as an open file report.

In the field, the locations of each outcrop encountered were recorded as GPS waypoints using the Gaia GPS iPhone application (<https://www.gaiagps.com/>). Each waypoint was labeled and assigned a unique color of symbol according to its specific lithology, which allowed for real time visualization of the spatial distribution of the various lithologic suites observed within the map area. The waypoints were then ultimately used to help make inferences regarding the placement of stratigraphic packages, contacts

between lithologies, and fault traces in order to construct a complete geologic map of the Mine Gulch USGS 7.5' quadrangle. Previously published maps by James (1990) and Garihan (1979) and their corresponding line and plate data were used to help supplement areas of the map that were not visited during the summer of 2017. ArcGIS was used to digitize the map for final submission, which will ensure the accuracy of the location of contacts between different lithologies as well as the placement of structural symbols.

In addition to the mapping of the Mine Gulch quadrangle, a total of 55 samples were collected from various structural levels within the map area during the summer of 2017. An emphasis was placed on the collection of metapelitic samples from each of the three major stratigraphic packages in the Ruby Range to be used for bulk rock geochemical analyses and P - T phase equilibria modeling.

4.2. Petrography

A total of 59 thin sections were prepared by Spectrum Petrographics from 46 samples collected during the summer of 2017 in addition to 13 samples that were previously collected during the summer of 2014. Twenty-eight of these thin sections were fashioned from different varieties of quartzofeldspathic gneiss, ultramafic rock, dolomitic and calcitic marbles, calc-silicate rock, mylonitic garnet leucogneiss, mylonitic garnet leucogneiss, mylonitized quartzite, and metaconglomerate in order to have additional representative thin sections of major units found within the Mine Gulch quadrangle. The remaining 31 thin sections were from metapelitic samples which were used to determine the best candidates for P - T phase equilibria modeling based on their peak assemblages and degree of alteration.

Samples were examined with a petrographic microscope. Thin section analysis was additionally supported by backscattered electron (BSE) images and energy dispersive X-ray spectroscopy (EDS) compositional maps obtained using the Tescan Vega-3 LM Scanning Electron Microscope (SEM)

equipped with an Oxford Instruments 80mm² X-Max SDD energy-dispersive analytical system housed in the Department of Geosciences at the University of Montana.

4.3. Bulk rock chemistry

Thirteen samples were selected for bulk rock geochemical analyses based on their peak mineral assemblages and stratigraphic position within the map area. Representative samples were trimmed from hand samples to remove weathered surfaces and to provide a homogeneous piece of rock for analysis. Samples were sent to Bureau Veritas, Vancouver, Canada to be processed and analyzed. Samples were then crushed, split, pulverized to 85% passing 150 μm mesh (PRP90-1KG) and analyzed by ICP-ES lithium borate fusion for major oxides which include: SiO_2 , Al_2O_3 , Fe_2O_3 , MgO , CaO , Na_2O , K_2O , TiO_2 , P_2O_5 , MnO , and Cr_2O_3 (LF300) (http://acmelab.com/pdfs/BVM_2017%20Fee%20Schedule.pdf for procedure and preparation references and details). The bulk chemistry for sample SW13-2, however, was measured off of its thin section using the EDS at the University of Montana. Bulk rock compositions can be found in tables 3 and 4.

4.4. Mineral chemistry

Mineral compositions were determined by calibrating the EDS to a range of natural mineral standards and were conducted *in situ* on polished thin sections. For garnet porphyroblasts, elemental X-ray compositional maps revealed chemical zonation which was used to guide the placement of spot analyses (Figure 7). All quantitative point analyses were performed at an accelerating voltage of 20 kV, a working distance of 15 mm, and a beam current of 2nA measured using a Faraday cup located on the sample holder with a live count time of 120 seconds. Results of mineral chemistry analyses can be found in tables 5 through 9.

Table 3.

Unnormalized, raw bulk rock compositions reported in weight% oxide. Sample SW13-2 is reported as normalized because its bulk chemistry was measured using SEM-EDS analysis off the thin section.

Sample	SiO₂	Al₂O₃	Fe₂O₃	FeO	MgO	CaO	Na₂O	K₂O	TiO₂	P₂O₅	MnO	Cr₂O₃
17-SS-8	55.11	21.92	10.09	9.08	3.96	0.40	1.04	3.31	0.72	0.08	0.10	0.030
17-SS-17	61.72	15.69	9.88	8.89	2.59	1.72	3.25	2.90	0.97	0.15	0.21	0.015
14-CH-9a	78.23	8.57	5.22	4.70	2.92	0.79	1.21	1.56	0.57	0.11	0.09	0.010
14-RG-01b	46.14	32.54	7.53	6.78	3.12	2.88	2.28	0.60	3.95	0.06	0.04	0.050
SC13-7	57.58	22.51	-	7.07	2.85	2.55	1.76	1.77	1.57	0.11	0.09	-
SW13-2*	69.75	9.41	-	11.08	4.14	0.50	0.01	3.28	1.24	0.60	0.01	-

*normalized

Table 4.

Normalized bulk rock compositions for THERMOCALC calculations reported in mol% oxide.

Sample	SiO₂	Al₂O₃	FeO	MgO	CaO	Na₂O	K₂O	TiO₂	O Value
17-SS-8	64.37	15.09	8.87	6.90	0.50	1.18	2.47	0.63	0.15
17-SS-17	65.65	9.83	7.91	4.11	1.96	3.35	1.97	0.78	0.14
14-CH-9a	79.96	5.16	4.01	4.45	0.87	1.20	1.02	0.44	0.15
14-RG-01b	54.74	22.75	6.72	5.52	3.66	2.62	0.45	3.53	0.15
SC13-7	57.02	13.14	5.85	4.20	2.70	1.69	1.12	1.17	0.15
SW13-2	73.97	5.88	9.83	6.55	0.57	0.00	2.22	0.99	0.15

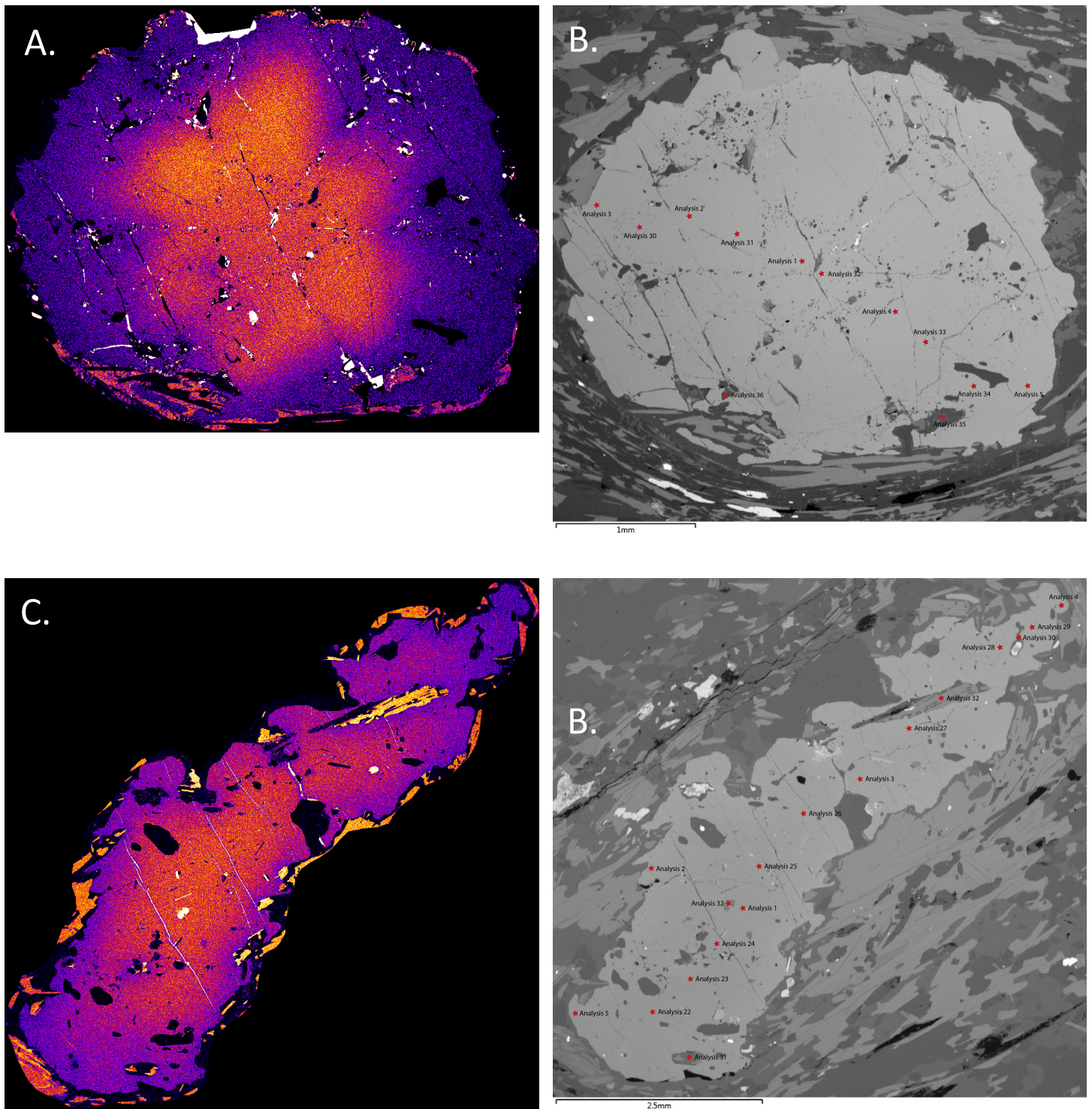


Figure 7. Examples of how elemental X-ray compositional maps of garnet revealed chemical zonation which was used to guide the placement of spot analyses for collecting mineral chemistry. **A)** Elemental map of Ca from a garnet from sample 17-SS-17. **B)** BSE image of the same garnet from 17-SS-17 depicting where spot analyses were placed (red stars) based on zonation patterns. A transect was made across the garnet in order to capture the transition of chemistry from the rim, to the core, and back to the rim. **C)** Elemental map of Mg from a garnet from sample SC13-7. **D)** BSE image of the same garnet from SC13-7 depicting placement of spot analyses. A similar rim-core-rim transect was made across the garnet.

4.5. Thermodynamic modeling

Pressure-temperature conditions for sillimanite-bearing metapelites were calculated for sample 14-CH-9a, SC13-7, 17-SS-17, SW13-2, RG-01b, and 17-SS-8 using the average P - T method of Powell & Holland (1994). Calculations were made using THERMOCALC v. 3.37 (Powell et al., 1998), and the internally consistent thermodynamic dataset 6.2 of Holland & Powell (2011). Calculations were undertaken in the Na_2O - CaO - K_2O - FeO - MgO - Al_2O_3 - SiO_2 - H_2O - TiO_2 - O_2 (NCKFMASHTO) chemical system. Mn was excluded because models for Mn-bearing endmembers for metapelitic minerals were originally calibrated from ideal-mixing models which are inconsistent with the non-ideal models used here (White et al., 2007). The activity composition (a - X) relationships used for phases involved in the pelite modeling include: garnet, biotite, staurolite, cordierite, chlorite, muscovite, paragonite, orthopyroxene, and silicate melt (White et al., 2014); plagioclase and K-feldspar (Holland and Powell, 2003); and ilmenite (White et al., 2000, 2014). The phases and phase abbreviations included in the modeling are (biotite (bi), chlorite (chl), cordierite (cd), garnet (g), ilmenite (ilm), K-feldspar (ksp), muscovite (mu), orthopyroxene (opx), paragonite (pa), plagioclase (pl), quartz (q), rutile (ru), silicate melt (liq), sillimanite/kyanite/andalusite (sill/ky/and), and staurolite (st).

Pseudosections were constructed from major element compositions based on ICP-ES whole rock geochemical analysis, except for sample SW13-2 whose bulk chemistry was measured from its thin section, as noted above. T - $X_{\text{H}_2\text{O}}$ diagrams were used to estimate $X_{\text{H}_2\text{O}}$ values which produces H_2O saturation at the solidus for each sample. In most cases, however, sub-solidus calculations were carried out using an $X_{\text{H}_2\text{O}}$ value of 50 to ensure complete saturation. T - X_{O_2} diagrams were additionally constructed in order to estimate the amount of ferric iron in the bulk composition of each sample. In terms of input into the script file, THERMOCALC deals with Fe_2O_3 as FeO and O (Diener and Powell, 2010). FeO is easily attainable seeing that it is either directly reported in the bulk chemistry results or

alternatively requires a simple calculation to convert from Fe_2O_3 (Fe_2O_3 value * 0.8998). This leaves estimating the amount of O, or ferric iron, which is strongly influenced by the oxide phases present in the sample (Diener and Powell, 2010). In all of the samples from this study which were modeled for P - T estimates, the most common oxide phases present are rutile and ilmenite, which indicates more reduced conditions (Diener and Powell, 2010). Therefore, for example, O values for 5 out of the 6 modeled samples were 0.15, and the remaining sample used an O value of 0.14.

5. Mapping results

Mapping of the Mine Gulch quadrangle associated with this study has produced two key observations which differ significantly from previously published maps of the region. The first primary distinction is how amphibolite bodies are mapped in the southern portion of the map area as part of the DG. In the map produced by James (1990), amphibolite in this portion of the quadrangle was mapped as very large, thick bodies. However, it has been determined that amphibolite in this area can be mapped at a much higher resolution by separating out the layers into thin, continuous beds that span the width of the quadrangle.

The second major finding is the separation of the garnet leucogneiss (GL) into its own distinct lithologic unit. The GL is a white, fine- to medium-grained garnet leucogneiss which is locally mylonitic (Figure 8). Outcrops of the mylonitic variety are distinguished by the presence of quartz ribbons and alkali feldspar augen (Figure 8). Previously, this unit has been mapped as part of the DG, however its leucocratic nature distinguishes it significantly from that of the nature of the other lithologies identified within the DG. This is significant because the unit implies that a widespread melting and metamorphic event occurred in the region. Not only has the GL been identified as intruding into the DG, but the unit also intrudes into the CRMS and the EGS throughout the entirety of the Ruby Range.

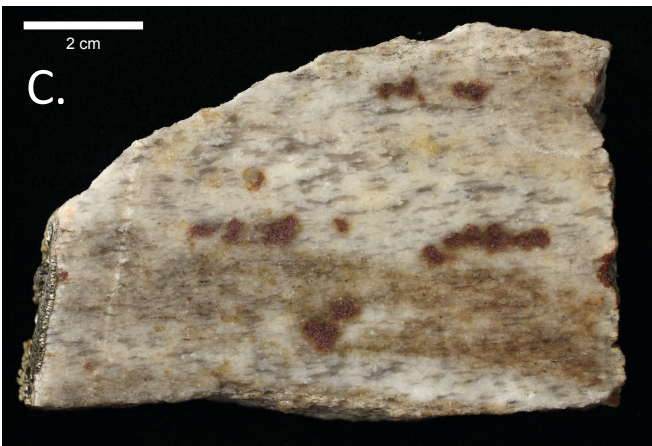


Figure 8. Field photographs and slabbed face images of the garnet leucogneiss (GL). **A & B)** Field photographs of GL outcrops. All outcrops encountered are generally very white in color due to the presence of plagioclase and quartz and are speckled with garnet porphyroblasts. The outcrop in image B is slightly more mylonitic than the outcrop in image A. **C)** Slabbed face image of mylonitic GL with prominent quartz ribbons.

New, additional foliation measurements have shown that all three of the primary units within the Mine Gulch quadrangle are very closely structurally related. An equal area stereogram from the CRMS show that poles to foliation define an average pole with a plunge 38° and a trend of 128° , and a stereogram from the DG show that poles to foliation define an average pole also with a plunge of 38° and a trend of 159° (Figure 9). This implies that all units exhibit evidence of an intertwined metamorphic history.

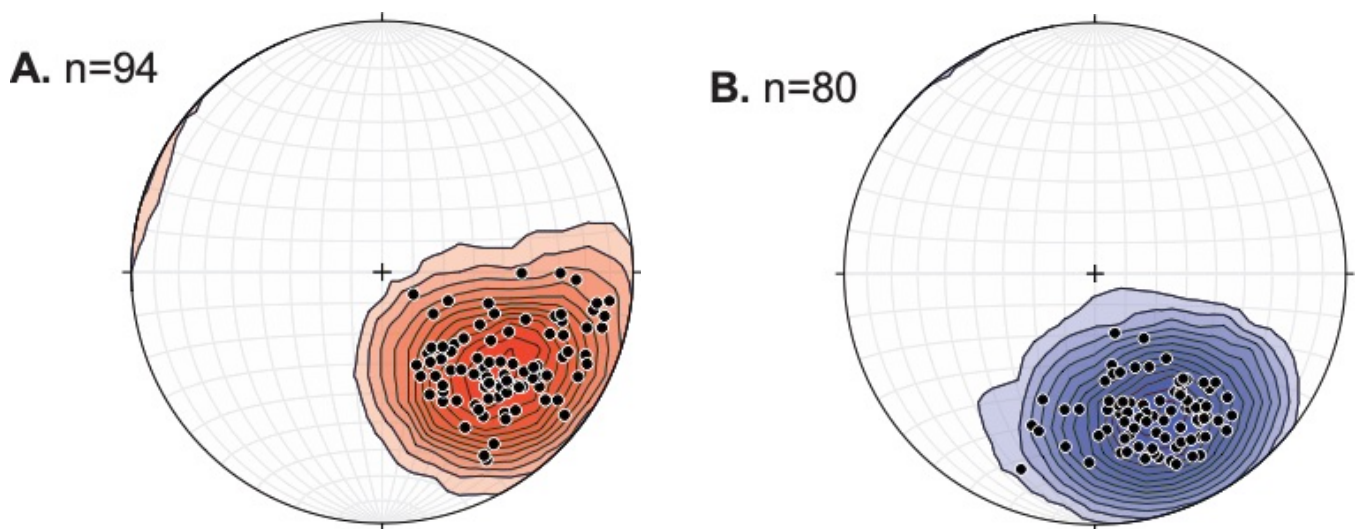


Figure 9. Equal area stereogram (lower-hemisphere projection) showing the poles to foliation measured from **A)** all units within the CRMS and adjacent quartzofeldspathic gneiss of the DG in the northwestern portion of the map area. Poles to foliation define an average pole that plunges 38° with a trend of 128° . **B)** Stereogram showing the poles to foliation measured from the DG in the southwestern portion of the map area west of the basalt flow. Poles to foliation define an average pole that plunges 38° with a trend of 159° .

6. Petrography

Three pelites from the CRMS, one pelite from the DG, and two pelites from the EGS were selected for petrographic modeling. Samples were selected based on the presence of ideal metamorphic mineral assemblages and textures suitable for P - T modeling in addition to a broad geographic distribution across the study area (Table 5). Additionally, samples were also carefully chosen to

Table 5.

sample location, sample mineralogy, and inferred peak assemblages.

Sample	Unit	Rock Type	GPS Coordinates UTM Zone 12		Mineralogy													Peak assemblage		
					Grt	Sil	Crd	Bt	Ms	St	Ksp	Pl	Qtz	Rt	Ilm	Ap	Mag		Mnz	Zrn
17-SS-8	CRMS	garnet-biotite-sillimanite schist	393063E	5009670N	x	x		x	T	T		x	x	x	x	x		x	x	Grt + Sil + Bt + Pl + Qtz + melt
14-CH-9a	CRMS	garnet-biotite-sillimanite schist	392187E	5008448N	x	x		x				x	x	x		x		x	x	Grt + Sil + Bt + Pl + Ilm + melt
17-SS-17	CRMS	garnet-biotite-sillimanite migmatitic gneiss	391958E	5004480N	x	x		x			x	x	x	x	x	x	x	x	x	Grt + Sil + Bt + Ksp + Pl + Ilm + melt
14-RG-01b	DG	garnet-biotite-sillimanite migmatitic gneiss	396655E	5010941N	x	x	R	x				x	x	x	x	x	x	x	x	Grt + Sil + Bt + Pl + Ru + melt
SC13-7	EGS	garnet-biotite-sillimanite gneiss	393849E	5007201N	x	x	R	x			x	x	x	x	x			x	x	Grt + Sil + Bt + Ksp + Pl + Ilm + Ru + melt
SW13-2	EGS	garnet-biotite-sillimanite schist	392149E	4997788N	x	x		x				x	x	x	x	x	x	x	x	Grt + Sil + Bt + Ilm + Ru + H2O

CRMS = Christensen Ranch metasedimentary suite, DG = Dillon Gneiss, EGS = older Elk Gulch Suite.

R = retrograde, S = sericitization, T = trace amount. Mineral abbreviations after Kretz (1983) and Evans (2010)

complement previously collected geochronology data. All samples are metapelitic, garnet-biotite-sillimanite bearing schists and gneisses \pm cordierite.

Partial melting produces large quantities of granitic melt in the Earth's crust which crystallizes in the rock to form leucosome. Leucosome is primarily composed of quartz, plagioclase feldspar, K-feldspar, and other minor components. The remainder, or the leftover from which the melts were extracted, is termed restite, and is generally comprised of more mafic minerals. In metapelites this is expressed as compositional layering of felsic phases (quartz, plagioclase and/or K-feldspar, sometimes sillimanite) vs. mafic phases (biotite, garnet, sillimanite). This layering can be observed at both the outcrop scale, in hand sample, and in thin section. The samples in this study exhibit varying degrees of migmatization, ranging from almost no evidence of migmatization in some schists to fully segregated melt bands in gneisses.

6.1. Sample 17-SS-8

Sample 17-SS-8 is a coarse garnet-biotite-sillimanite schist collected from the middle CRMS located in the northwestern corner of the Mine Gulch quadrangle on the western flank of the range (Figure 10). The exposure is approximately ~5-10 m thick and occurs as an isolated outcrop located on the northern flank of a shallow gully.

The observed mineral assemblage in this sample is characterized by medium- to coarse-grained garnet, sillimanite, biotite, plagioclase, and quartz; minor traces of muscovite, staurolite, rutile, magnetite, and apatite; additional secondary chlorite and accessory tourmaline (Figure 11c). Subhedral garnet occurs as 3-8 mm, highly fractured and weathered porphyroblasts with inclusions of quartz, biotite, sillimanite, plagioclase, apatite, staurolite, monazite, zircon, and rutile (Figure 11a). All inclusions exhibit a random orientation, which suggests that garnet growth initiated prior to deformation.

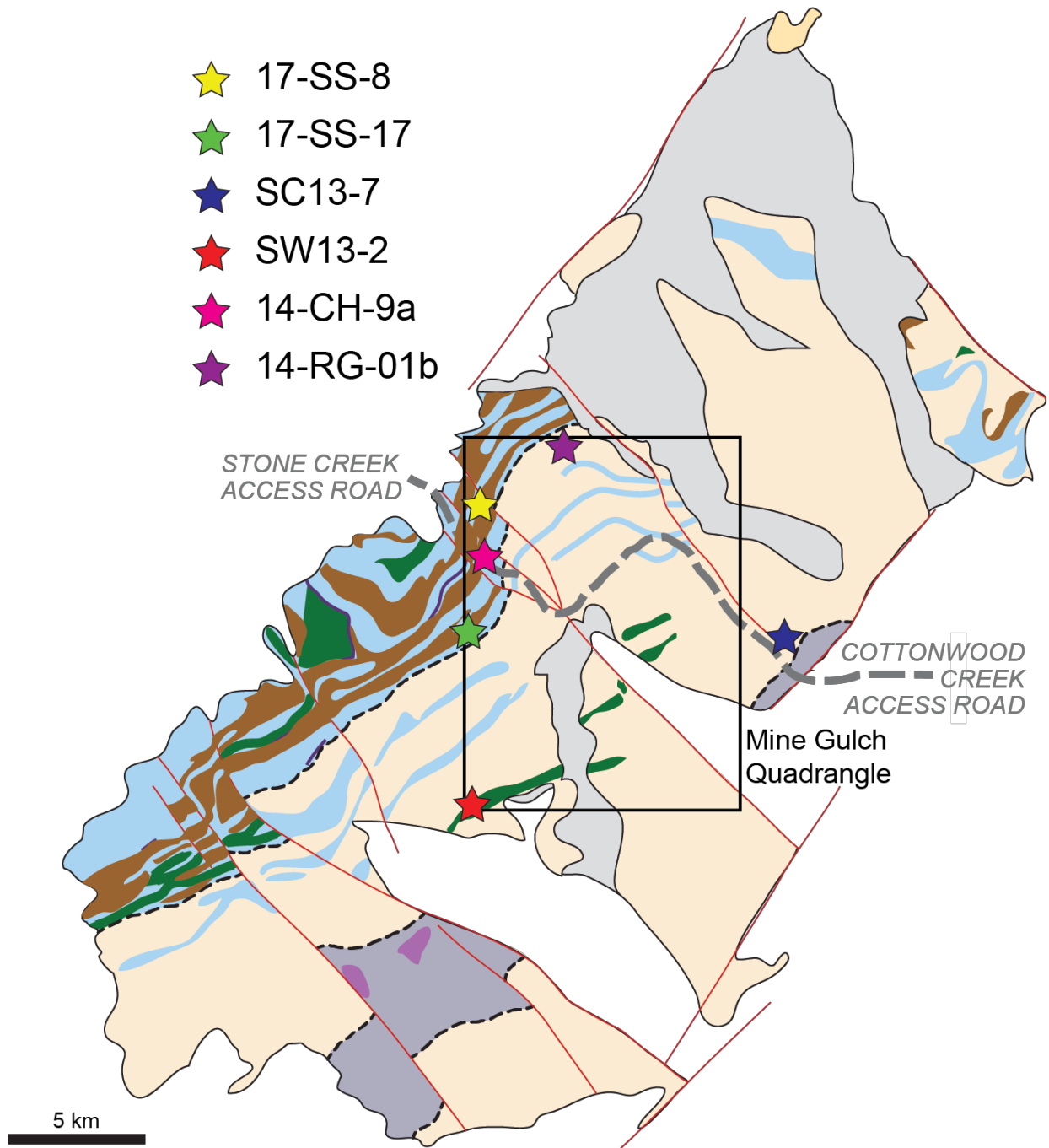


Figure 10. Simplified geologic map of the Ruby Range showing locations of each sample chosen for petrographic modeling.

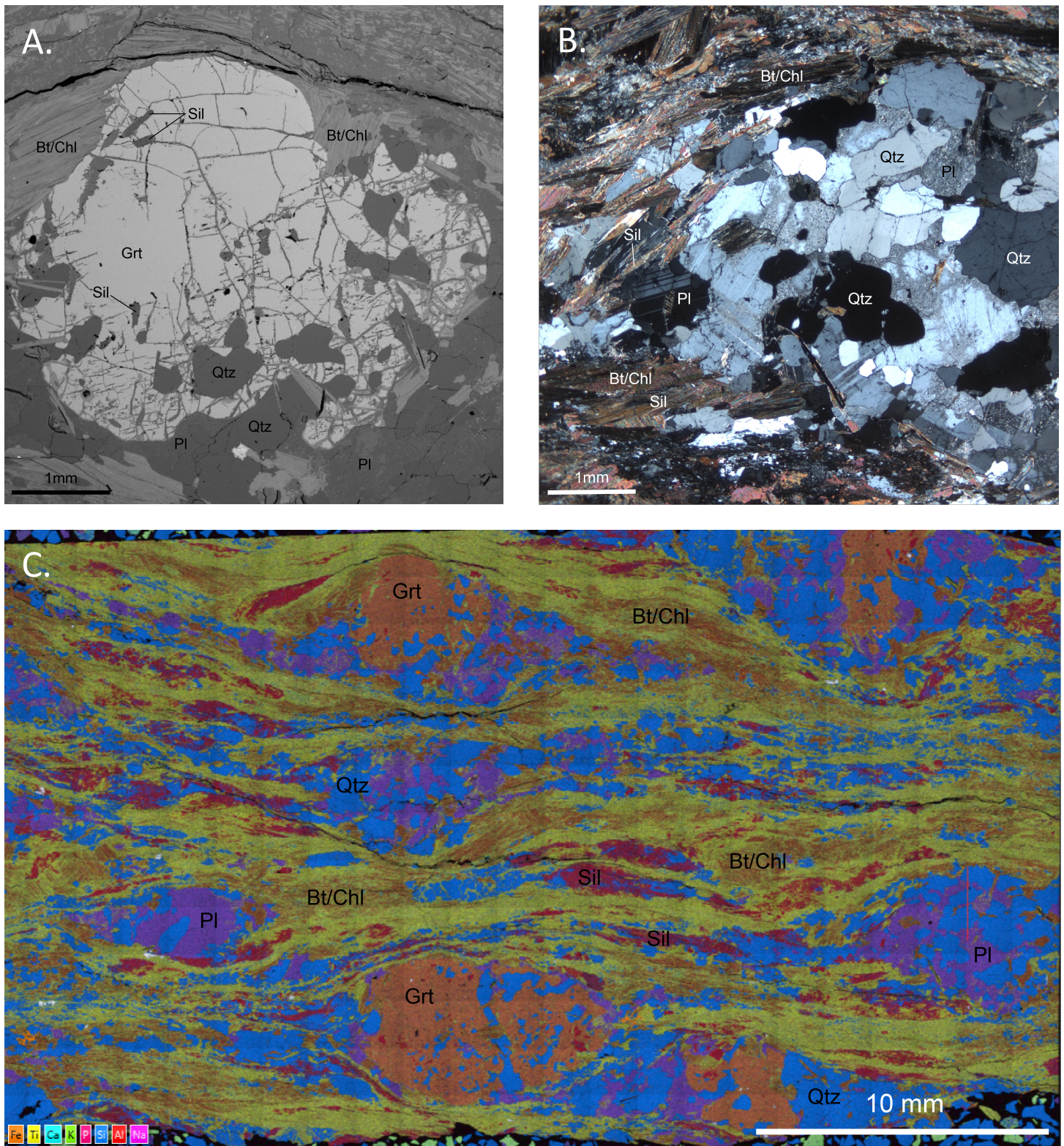


Figure 11. Photomicrograph, backscattered electron (BSE), and energy dispersive x-ray spectrometry (EDS) images from sample 17-SS-8. **A)** BSE image of representative garnet from the sample which exhibits the highly fractured and weathered nature of the grains. **B)** XPL image of melt region within thin section. Defined by “pods” of quartz and plagioclase, which is often sericitized. Such regions of melt occur commonly throughout the sample. **C)** Full section EDS scan of sample 17-SS-8. Garnet is orange, quartz is blue, plagioclase is purple, sillimanite is red, and green/red regions are biotite with secondary chlorite alteration. Areas of melt are represented by “pods” of plagioclase and quartz in purple and blue, respectively.

Biotite and sillimanite define the foliation of the sample and often wrap garnet, commonly forming tails around strain shadows. Approximately 75% of biotite in the sample has been altered to chlorite, which occurred as a result of retrograde metamorphism. Sillimanite occurs within the matrix as well as inclusions in garnet as prismatic aggregates, comprising ~20% of the total rock by volume. Occasionally, sillimanite occurs as elongated, bladed needles. Melt is inferred from the presence of ~5-8 mm x ~2-5 mm pods of plagioclase, which is often sericitized, and quartz visible at both the outcrop and thin section scale (Figure 11b). Oxide phases are relatively uncommon within the sample; only a few rutile and magnetite grains were identified within the matrix. However, a handful of magnetite grains were identified as inclusions within garnet. Monazite and zircon primarily occur within the matrix of the sample, although one or two grains of each mineral were identified as inclusions within garnet. Apatite occurs as inclusions within garnet but more commonly within the matrix of the rock, reaching lengths of 0.7 mm. Muscovite is also present in the sample in trace amounts; grains were recognized near the edge of one of the garnet porphyroblasts and in the matrix. A single 1 mm tourmaline grain was identified at the edge of a garnet grain by its olive-green pleochroism in plane-polarized light and uniaxial negative optical sign. Staurolite occurs as 0.1-0.5 mm inclusions within garnet and is not found within the matrix of the sample. Based on these observations, the peak metamorphic assemblage is interpreted as garnet + sillimanite + biotite + plagioclase + melt.

6.2. Sample 14-CH-9a

Sample 14-CH-9a is a medium- to coarse-grained garnet-biotite-sillimanite schist collected from the middle CRMS located on the south-facing slope of a ridge just north of Stone Creek Road (Figure 10). The outcrop was approximately 50 cm thick, and is bound above and below by biotite banded gneiss.

The observed mineral assemblage in 14-CH-9a is characterized by medium-grained garnet, biotite, plagioclase, and quartz with minor amounts of sillimanite, apatite, rutile, monazite, and zircon (Figure 12c). Subhedral to anhedral garnet occurs as 0.8-2.5 mm porphyroblasts and porphyroblast clusters with inclusions of quartz, biotite, apatite, monazite, zircon, and rutile (Figure 12a). All inclusions exhibit a random orientation, suggesting that garnet growth initiated prior to deformation. Quartz is the dominant phase in the sample, comprising almost 70% of the thin section by volume, followed by plagioclase (15%) and biotite (10%). The foliation in this sample is relatively weak compared to other samples in the study but is defined primarily by biotite and sillimanite. Sillimanite occurs exclusively within the matrix of the sample as primarily prismatic needles but also as rectangular crystals, comprising only 1-2% of the total rock by volume. Melt is inferred by bands/regions of plagioclase and quartz (Figure 12b). Rutile is the only phase identified within the sample, occurring both in the matrix and as inclusions in garnet ranging from 28 μm to ~ 1.8 mm in diameter. Both monazite and zircon occur in the matrix as well as inclusions within garnet, where zircon tends to be substantially smaller than monazite but more abundant. Apatite also occurs in both the matrix and as inclusions in garnet, and ranges from 0.15-0.4 mm in diameter.

6.3. Sample 17-SS-17

Sample 17-SS-17 is a garnet-biotite-sillimanite migmatitic gneiss collected from the base of the CRMS located along the westernmost edge of the Mine Gulch quadrangle (Figure 10). The exposure exhibits significant signs of weathering and occurs adjacent to a remote ~ 10 m thick lens of calcitic marble.

The observed mineral assemblage in this sample is characterized by fine- to medium-grained garnet, biotite, sillimanite, plagioclase, K-feldspar, and quartz; minor amounts of rutile, ilmenite,

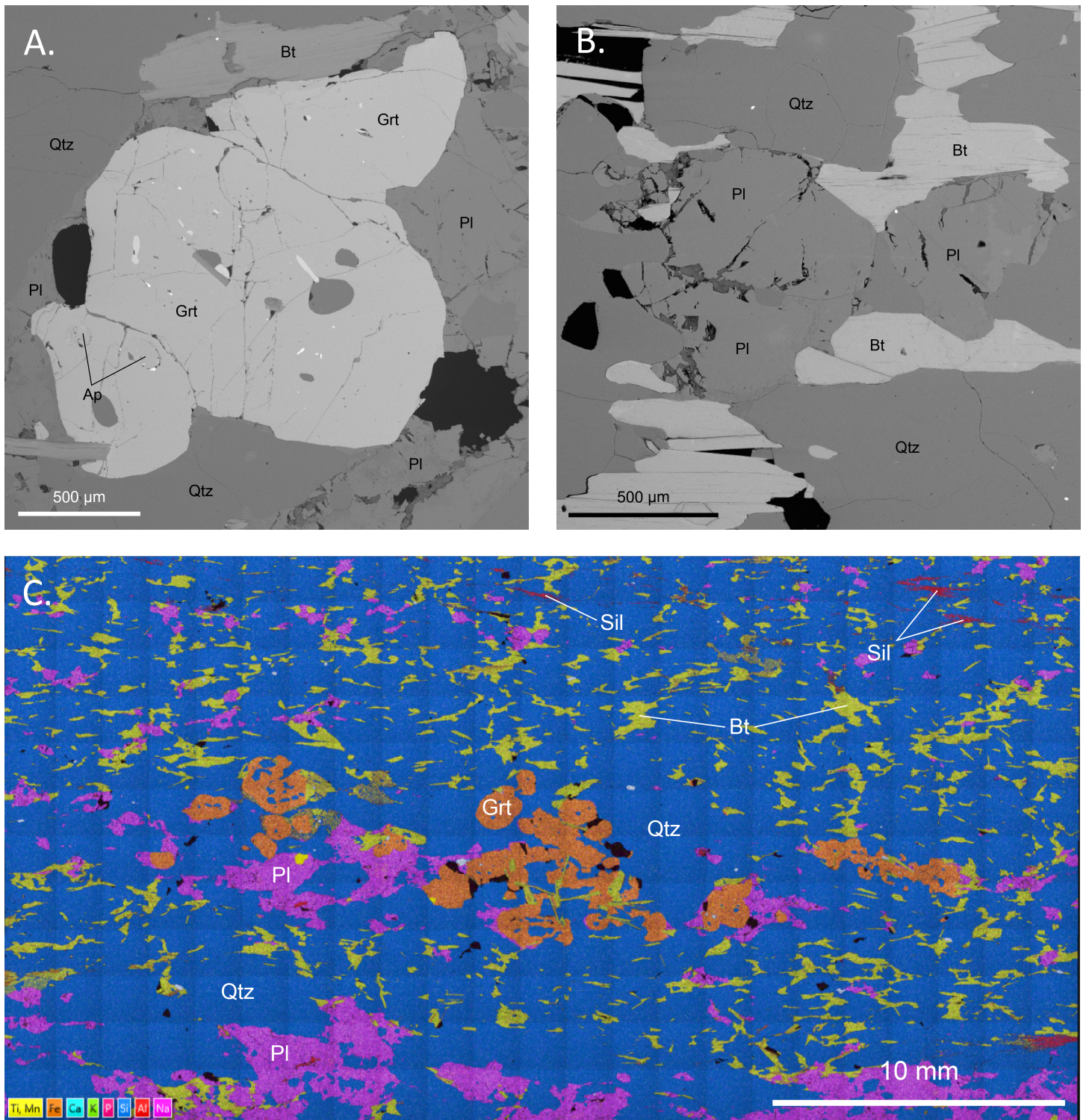


Figure 12. BSE and EDS images from sample 14-CH-9a. **A)** BSE image of example garnet porphyroblast cluster exhibiting anhedral – subhedral shape and random inclusion pattern. **B)** BSE image of characteristic texture within the sample. Quartz is the dominant phase in the matrix, and the foliation is defined by the alignment of biotite. **C)** Full section EDS scan of sample 14-CH-9a. Garnet is orange, quartz is blue, plagioclase is purple, biotite is green, and sillimanite is red. The bottom half of the thin section image is representative of a melt band based on the higher percentage of plagioclase present in conjunction with quartz.

magnetite, apatite, monazite, and zircon; trace amounts of tourmaline and baryte (Figure 13c). Euhedral to anhedral garnet occurs as ~1.5-3.5 mm inclusion rich porphyroblasts (Figure 13a). Inclusions in garnet include quartz, biotite, plagioclase, monazite, zircon, apatite, sillimanite, rutile, and magnetite. Inclusion trails within the cores of garnet located in the neosome reveal synkinematic rotation during deformation. Inclusions within garnet in the paleosome display a random orientation suggesting that garnet growth initiated prior to deformation. The foliation is defined by the alignment of biotite and sillimanite, which slightly wrap only a fraction of garnet porphyroblasts in the sample (Figure 13b). Sillimanite tends to occur as prismatic crystals which form in narrow yet distinct, discontinuous bands across the sample. Biotite is prevalent throughout the entirety of the sample but exhibits a coarser texture within the neosome as opposed to the paleosome, comprising ~20% of the sample by volume. Both plagioclase (~20% of sample by volume) and K-feldspar (~8% of sample by volume) occur throughout the sample as discrete grains, however K-feldspar is more prevalent and coarser grained within the neosome. Rutile is the most abundant oxide phase identified within the sample and is found as inclusions within garnet but more commonly within the matrix reaching lengths of ~0.5 mm. Ilmenite is only slightly less common within the sample, and occurs primarily in the matrix but also as inclusions within garnet, reaching maximum lengths of ~0.9 mm. Scarce magnetite grains have also been identified within the sample, occurring in both the matrix and as inclusions within garnet. The remainder of accessory phases, monazite, zircon, apatite, and trace amounts of tourmaline additionally occur as inclusions within garnet and within the matrix of the sample.

6.4. Sample SC13-7

Sample SC13-7 is a garnet-biotite-sillimanite-cordierite gneiss collected from the EGS located just off the eastern edge of the Mine Gulch quadrangle along Cottonwood Creek Road (Figure 10).

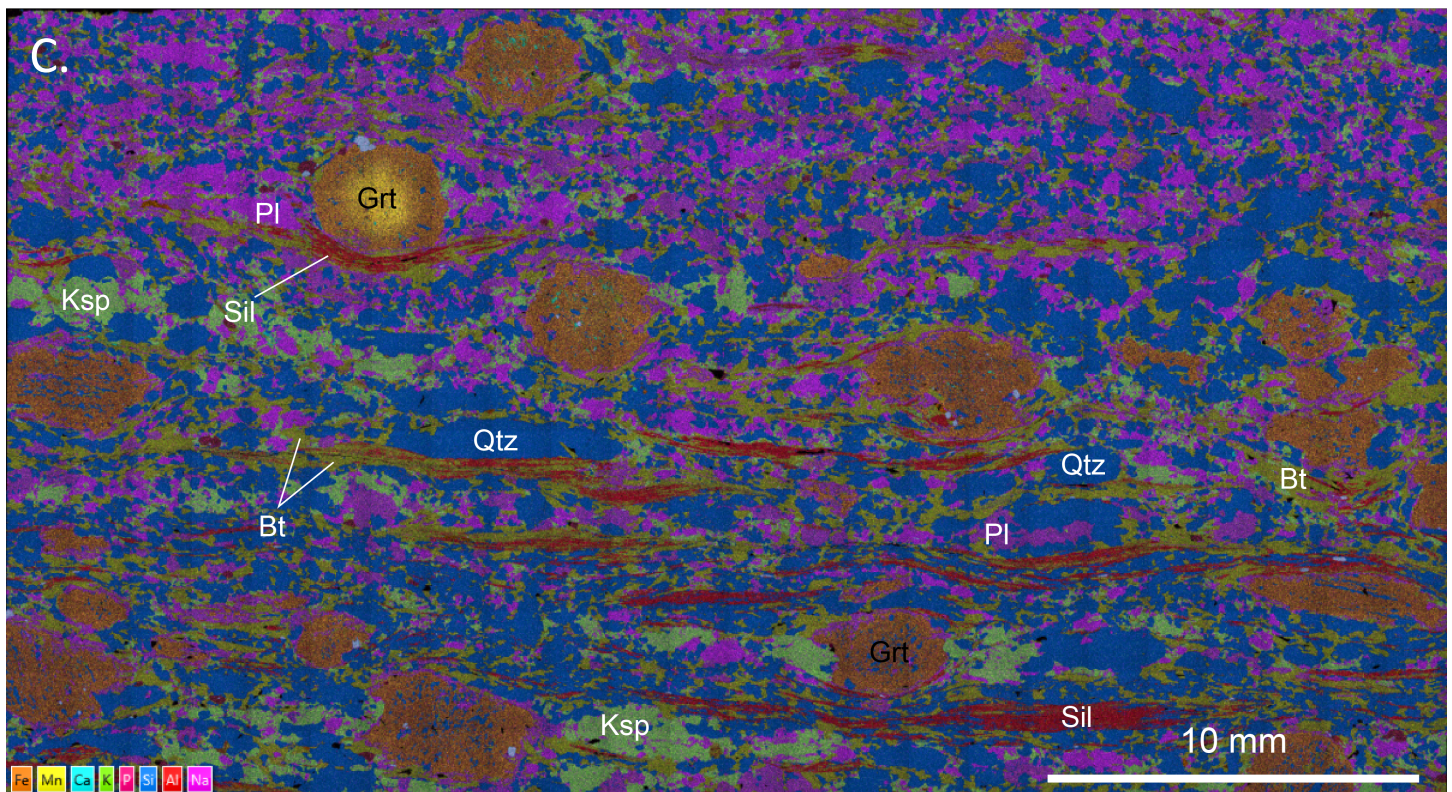
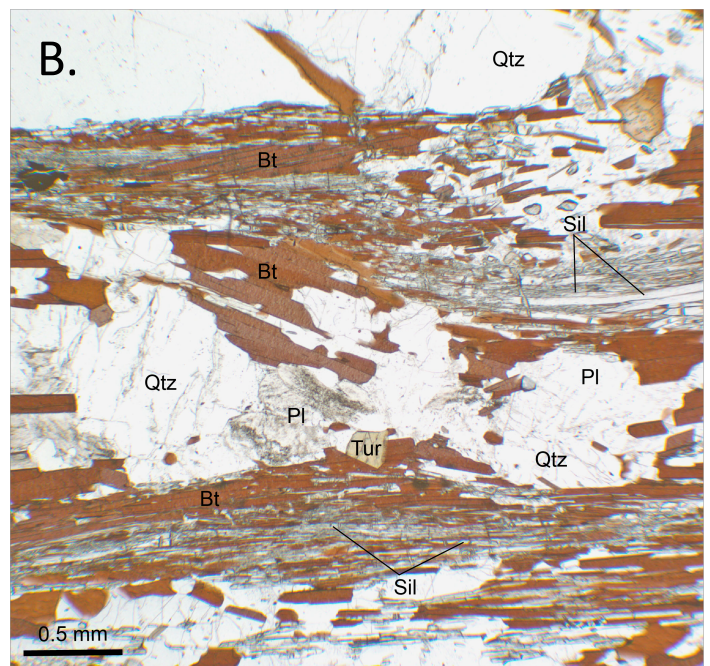
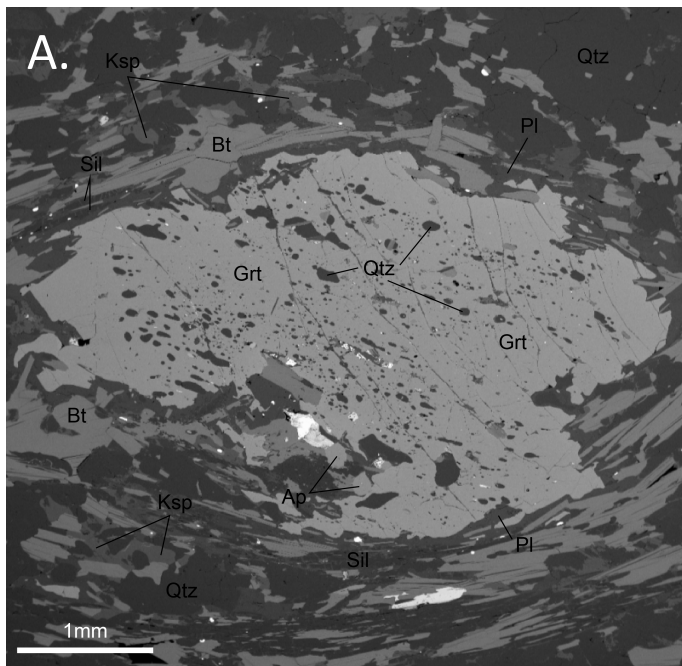


Figure 13. BSE, photomicrograph, and EDS images from sample 17-SS-17. **A)** BSE image of a single garnet grain which exhibits inclusion trails. The majority of garnet in the sample display evidence of synkinematic rotation, however a few garnets exhibit inclusions of random orientation inferring multiple episodes of garnet growth. **B)** PPL photomicrograph showing prismatic, bladed sillimanite texture which aids in defining the foliation of the sample. Image also displays regions of melt represented by pods of plagioclase and quartz. **C)** Full section EDS scan of sample 17-SS-17. Garnet is orange, quartz is blue, biotite is yellow-green, K-feldspar is green, plagioclase is purple, and sillimanite is red. Multiple generations of garnet growth are evident based on differences in inclusion patterns as well as zoning in garnet in the upper left-hand corner. Melt layer is inferred by the region in the bottom half of the thin section which is dominated by quartz, plagioclase, and K-feldspar.

The observed mineral assemblage in SC13-7 is characterized by medium- to coarse-grained garnet, biotite, sillimanite, plagioclase, quartz, and cordierite; minor amounts of rutile, ilmenite, apatite, monazite, and zircon (Figure 14c). Subhedral to anhedral garnet occurs as ~1.2-8 mm inclusion rich porphyroblasts (Figure 14a). Inclusions in garnet include sillimanite, biotite, plagioclase, quartz, rutile, ilmenite, monazite, zircon, and cordierite. All inclusions exhibit a random orientation, suggesting that garnet growth initiated prior to deformation. Garnet growth occurs primarily within the paleosome but does occur less commonly within the neosome. By volume, the sample is comprised of approximately 30% plagioclase, 30% quartz, 8% biotite, and 8% sillimanite. Sillimanite tends to occur as both blocky and prismatic crystals within the matrix, more commonly in the paleosome than the neosome, but also as inclusions within garnet. Biotite is profoundly more common within restitic portions of the sample but does occur in small quantities within the leucosome. Melt is inferred by the presence of plagioclase, which is often sericitized, and quartz rich bands that span across the sample. However, both minerals are additionally present within the restitic portion of the rock. Both ilmenite and rutile occur abundantly throughout the paleosome while only a handful of either minerals were identified within melt layers. Similarly, monazite and zircon occur throughout the sample and as inclusions within garnet but are found in greater concentrations within the paleosome. Apatite is present as inclusions in garnet but more commonly found within the matrix of the sample, reaching maximum lengths of approximately ~0.4 mm. Cordierite occurs primarily as halos around approximately half of the garnet grains in the sample, but also as an inclusion within one of the garnet grains (Figure 14b). Additionally, cordierite is often pseudomorphed by pinitite when found in the matrix.

6.5. Sample SW13-2

Sample SW13-2 was collected from the EGS located along Sweetwater Creek road near the

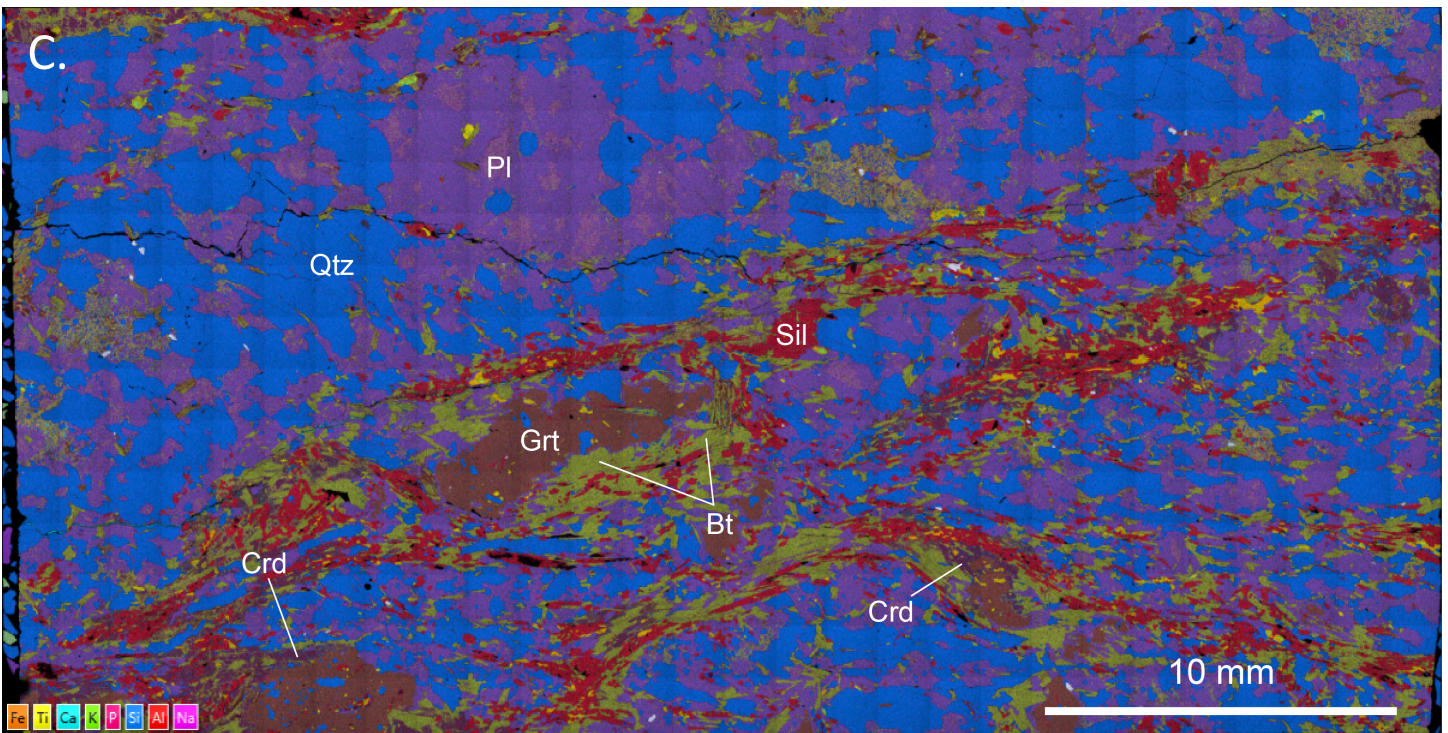
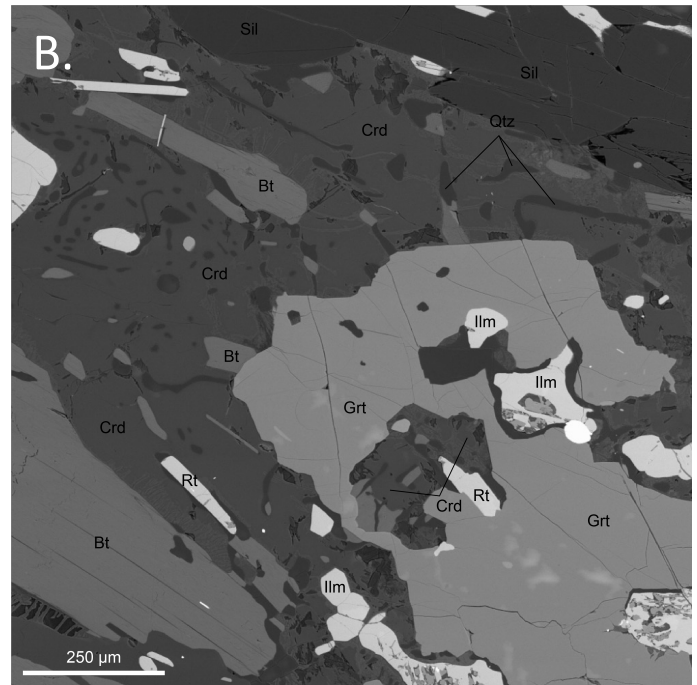
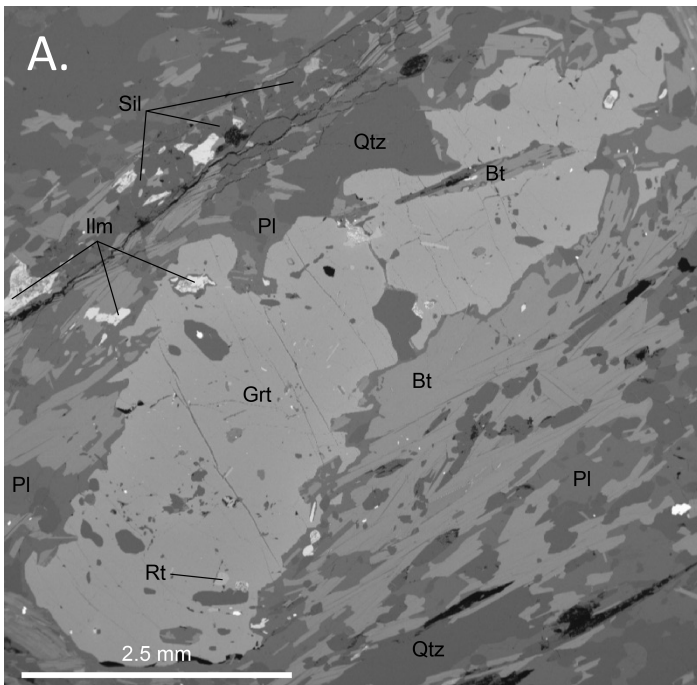


Figure 14. BSE and EDS images from sample SC13-7. **A)** BSE image of anhedral garnet porphyroblast exhibiting random inclusion orientation. Image also displays how biotite and sillimanite tend to wrap the garnet grains and aid in defining the foliation. **B)** BSE image of retrograde cordierite halo around garnet rim. Cordierite halos occur around most garnet in the sample, but also occur less commonly as inclusions within garnet. **C)** Full section EDS scan of sample SC13-7. Garnet is orange, quartz is blue, biotite is green, plagioclase is purple, and sillimanite is red. The image shows distribution of melt bands, evidenced by the upper half of the slide which is characterized by a dominance of plagioclase and quartz in addition to a lack of garnet and sillimanite.

southwestern corner of the Mine Gulch quadrangle (Figure 10).

The observed mineral assemblage in SW13-2 is characterized by medium- to coarse-grained garnet, biotite, quartz, and sillimanite; minor amounts of rutile, ilmenite, magnetite, monazite, zircon and apatite (Figure 15c). Subhedral to anhedral garnet occurs as ~1-6 mm inclusion rich porphyroblasts (Figure 15a). Inclusions in garnet include quartz, biotite, ilmenite, rutile, apatite, monazite, and zircon. Inclusions in garnet exhibit a random orientation, which suggests garnet growth initiated prior to deformation. This sample does not contain feldspar, indicating that this sample did not experience pressures and temperatures great enough to generate melt. By volume, the sample is comprised of approximately 44% quartz, 40% biotite, and 13% garnet, and only ~1% sillimanite. Sillimanite occurs exclusively in the matrix, and exists primarily as prismatic, blocky crystals, but also as elongated prismatic needles. Occasionally, sillimanite can be found near the grain boundaries of garnet, but never fully wraps the porphyroblasts. Biotite is prevalent throughout the sample, primarily blocky in shape, and also occurs as inclusions within garnet (Figure 15b). The distribution of ilmenite, rutile, magnetite, monazite, and zircon throughout the sample is sparse, however all occur as inclusions in garnet as well as in the matrix of the sample and are less than ~0.15 mm in length. Apatite is commonly found throughout the sample as both inclusions in garnet and in the matrix, reaching lengths of ~1 mm.

6.6. Sample 14-RG-01b

Sample 14-RG-01b is the leucocratic portion of a pelitic migmatite collected from the DG at a location referred to as “Top of the Range” (Figure 10). The outcrop is bound above and below by two distinct amphibolite layers, each with thicknesses of approximately 5 m. In outcrop, leucocratic material generally occurs as gneissic bands ranging from 1-5 cm in thickness, but also occurs as discontinuous lenses interspersed with melanocratic material.

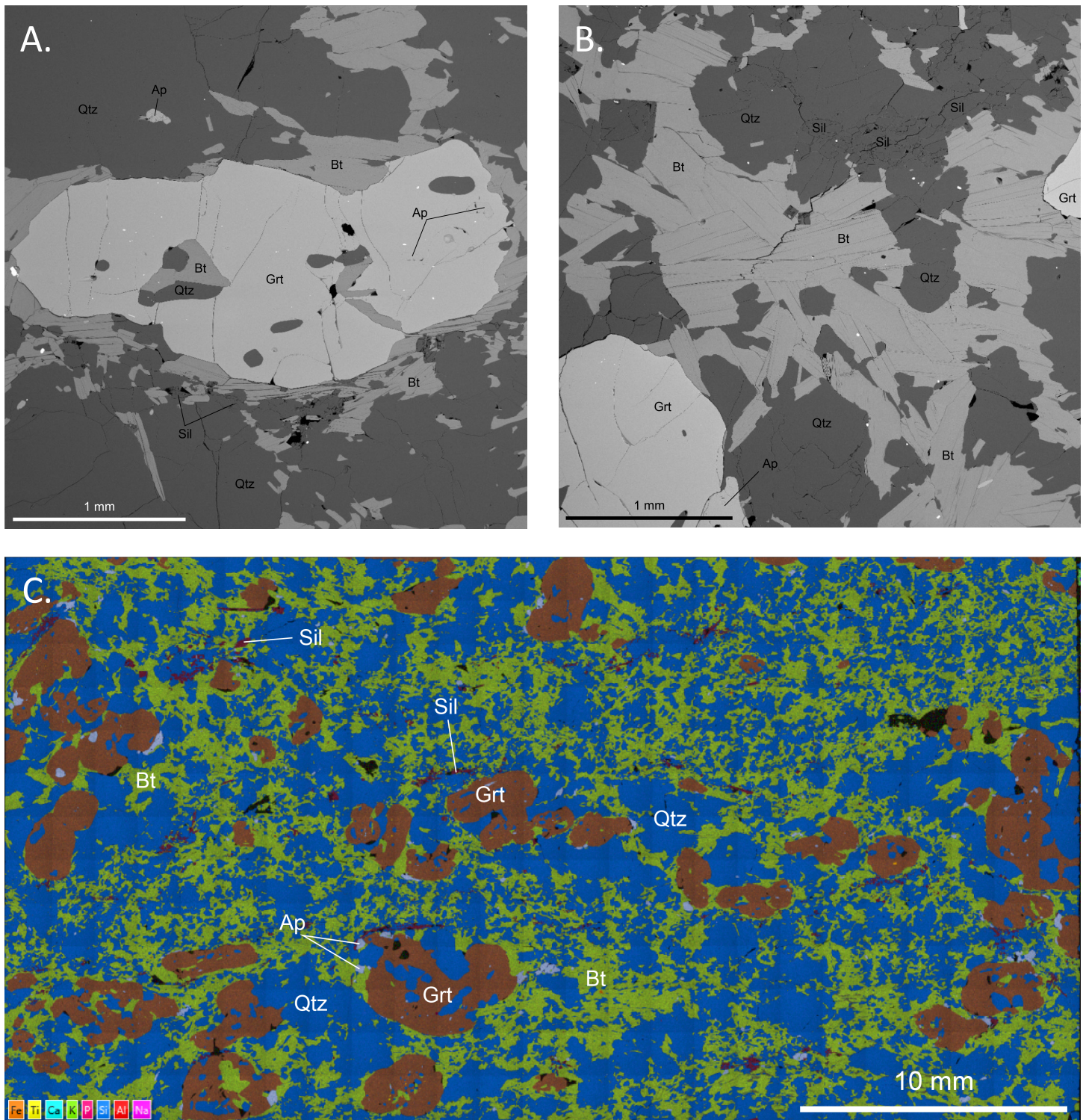


Figure 15. BSE and EDS images from sample SW13-2. **A)** BSE image of anhedral garnet porphyroblast which exhibits random inclusion orientations. Garnet in this sample is often wrapped by biotite, and in rare cases, minor amounts of sillimanite. **B)** BSE image displaying typical texture observed throughout the sample which is comprised of biotite and quartz. Minor amounts of blocky sillimanite grains are present within the image. **C)** Full section EDS scan of sample SW13-2. Garnet is orange, quartz is blue, biotite is green, sillimanite is red, and apatite is light blue. The image aids in illustrating the lack of plagioclase identified within the sample, which also correlates to the very minor amount of melt produced in the sample.

The observed mineral assemblage in this sample is characterized by fine-grained garnet, biotite, plagioclase, and sillimanite; minor amounts of quartz, ilmenite, rutile, magnetite, apatite, cordierite, monazite, and zircon (Figure 16c). Mineral percentages in the sample by volume are as follows: ~60% plagioclase, ~12% garnet, ~10% sillimanite, ~10% biotite, ~1% quartz, and the remaining ~7% minor and accessory phases. Subhedral to anhedral garnet occurs as 0.3-3.5 mm inclusion rich porphyroblasts (Figure 16a). Inclusions in garnet include biotite, sillimanite, quartz, plagioclase, rutile, ilmenite, monazite, and zircon. All inclusions in garnet have a random orientation, suggesting garnet growth initiated prior to deformation. Sillimanite is generally prismatic and is on average ~0.4 mm in diameter with seemingly random orientations throughout the thin section. Biotite is well distributed throughout the sample and occurs as blocky, prismatic grains, also lacking a well-defined orientation. 14-RG-01b has the highest concentration of oxide phases out of all samples examined in this study. Rutile is the most common oxide phase that occurs within the sample and is very widespread as both inclusions in garnet and throughout the matrix. Ilmenite is significantly less common in comparison to rutile and tends to occur more commonly in the matrix as opposed to as inclusions in garnet. Cordierite occurs as halos around a handful of garnet grains in the sample, and also as scarce inclusions within garnet (Figure 16b). Only a handful of apatite grains exist within the sample, and occur exclusively within the matrix of the sample reaching a maximum diameter of 0.15 mm. Monazite and zircon are both prevalent throughout the sample, however zircon tends to be found as inclusions within garnet more commonly than monazite.

7. Mineral Chemistry

Representative mineral chemistry analyses for samples 17-SS-8, 14-CH-9a, 17-SS-17, SC13-7, SW13-2, and 14-RG-01b are presented in Tables 6 through 9.

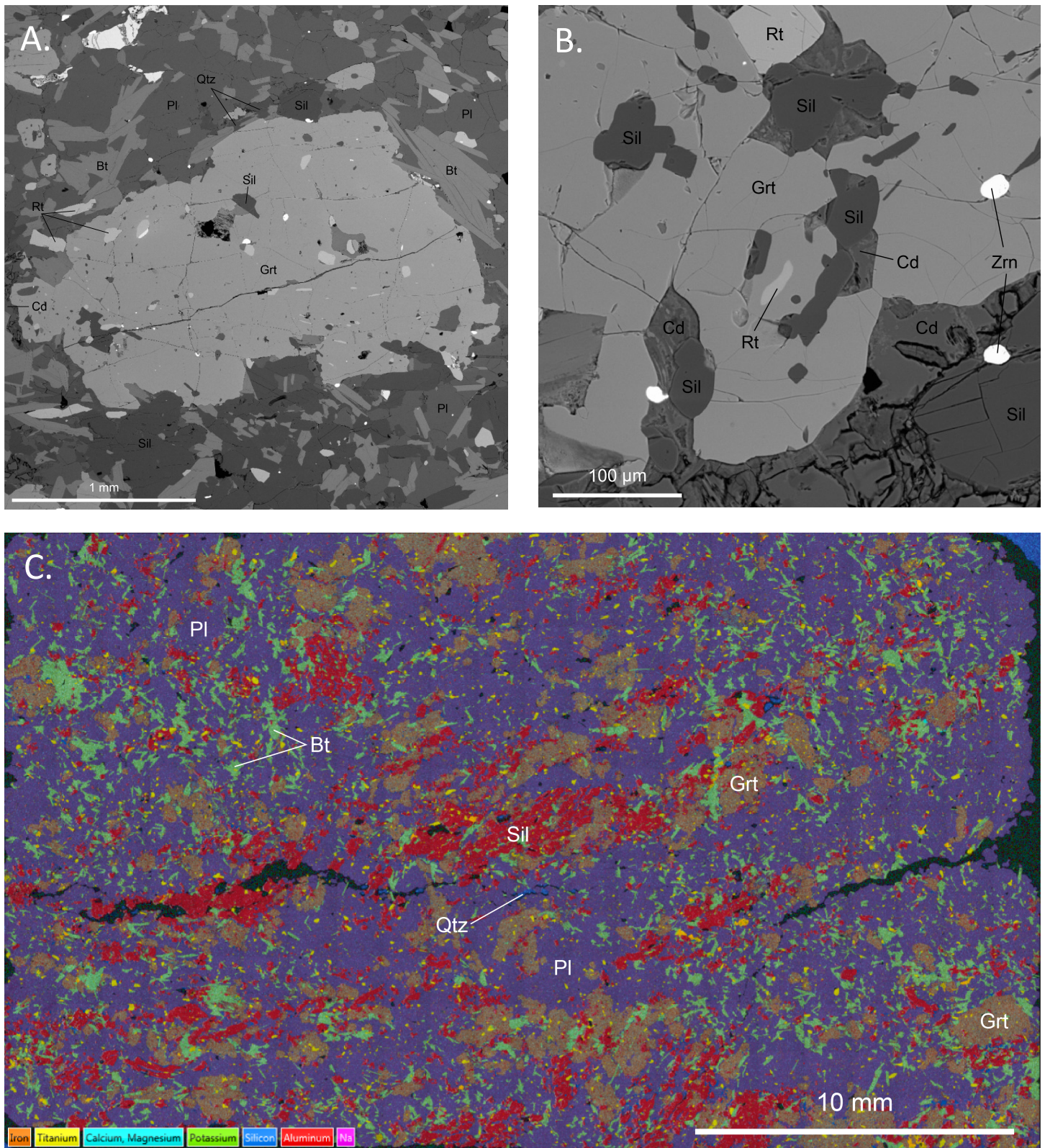


Figure 16. BSE and EDS images from sample 14-RG-01b. **A)** BSE image of anhedral garnet porphyroblast with random inclusion orientation. **B)** Example texture of a retrograde cordierite halo around a garnet grain. Approximately half of garnet grains in the sample have a cordierite halo, and when present is generally very thin and altered to pinite. **C)** Full section EDS scan of sample of sample 14-RG-01b. Garnet is orange, biotite is green, sillimanite is red, and quartz is blue. Matrix of sample is almost entirely composed of plagioclase with only ~1% quartz.

7.1. Sample 17-SS-8

Garnet in sample 17-SS-8 is $\text{Alm}_{0.70-0.76}\text{Prp}_{0.19-0.25}\text{GrS}_{0.02-0.04}\text{SpS}_{0.02}$. Garnet cores are unzoned, with $X_{\text{Fe}} = 0.74-0.75$ where $X_{\text{Fe}} = \text{Fe}^{2+} / (\text{Fe}^{2+} + \text{Mg})$. Narrow rims are slightly enriched in Fe and depleted in Mg, with $X_{\text{Fe}} = 0.79-0.80$. Fe-Mg zoning in the rims is consistent with diffusive re-equilibration during resorption. Ca is unzoned, with $X_{\text{Ca}} = 0.02-0.03$ where $X_{\text{Ca}} = \text{Ca} / (\text{Ca} + \text{Mg} + \text{Fe}^{2+})$. The composition of biotite grains in the matrix is $X_{\text{Fe}} = 0.46$, however the composition of biotite inclusions in garnet are slightly depleted in Fe and range from $X_{\text{Fe}} = 0.28-0.38$ for 5 inclusions from 3 different garnet porphyroblasts. The composition of plagioclase in the matrix ranges from $X_{\text{An}} = 0.13-0.15$, where $X_{\text{An}} = \text{Ca} / (\text{Na} + \text{Ca} + \text{K})$. Three out of seven plagioclase inclusions within garnet have compositions of $X_{\text{An}} = 0.15$, and the remaining four inclusions have compositions of $X_{\text{An}} = 0.00$.

7.2. Sample 14-CH-9a

Garnet in sample 14-CH-9a is $\text{Alm}_{0.65-0.69}\text{Prp}_{0.24-0.30}\text{GrS}_{0.03-0.04}\text{SpS}_{0.02-0.03}$. Garnet cores are unzoned with $X_{\text{Fe}} = 0.69-0.70$ and $X_{\text{Ca}} = 0.03-0.04$. Rims are slightly enriched in Fe^{2+} and depleted in Mg yielding a composition $X_{\text{Fe}} = 0.70-0.74$. Fe-Mg in the narrow rims is consistent with diffusive re-equilibration during resorption. The composition of biotite inclusions in garnet is $X_{\text{Fe}} = 0.25$, whereas matrix biotite grains reveal more Fe-rich compositions ranging from $X_{\text{Fe}} = 0.35-0.38$. Plagioclase was not identified as inclusions within garnet, however the composition of plagioclase in the matrix exhibited compositions of $X_{\text{An}} = 0.23-0.25$.

7.3. Sample 17-SS-17

Garnet in sample 17-SS-17 is $\text{Alm}_{0.54-0.73}\text{Prp}_{0.11-0.21}\text{GrS}_{0.05-0.17}\text{SpS}_{0.03-0.18}$. The majority of garnet porphyroblasts in the sample exhibit narrow rims slightly enriched in Fe ($X_{\text{Fe}} = 0.81-0.82$) and depleted

Table 6.
Representative garnet SEM-EDS analyses

Sample	17-SS-8	17-SS-8	14-CH-9a	14-CH-9a	17-SS-17	17-SS-17	SC13-7	SC13-7	SW13-2	SW13-2	14-RG-01b	14-RG-01b
Setting	Core	Rim	Core	Rim	Core	Rim	Core	Rim	Core	Rim	Core	Rim
SiO₂	37.99	37.71	38.93	38.79	37.80	37.88	38.67	37.95	38.36	38.06	38.73	38.38
TiO₂	0.02	0.03	0.02	0.03	0.01	0.01	0.03	0.01	0.01	0.00	0.00	0.04
Al₂O₃	21.51	21.44	21.78	21.61	21.43	21.49	21.78	21.34	21.61	21.56	21.89	21.79
FeO	32.82	34.21	29.83	30.74	31.71	32.64	31.36	33.70	33.91	34.95	28.52	31.24
MgO	6.10	4.76	7.24	6.63	5.26	4.39	6.48	4.35	5.59	4.77	8.41	6.52
MnO	0.74	1.10	1.10	1.29	1.41	2.05	0.55	0.92	0.39	0.40	0.23	0.31
CaO	0.71	0.75	1.50	1.16	2.00	1.92	1.97	1.88	0.87	0.85	1.76	1.75
Σ	99.89	100.00	100.40	100.25	99.62	100.38	100.84	100.15	100.74	100.59	99.54	100.03
Si	3.000	3.001	3.020	3.027	3.000	3.002	3.006	3.014	3.011	3.008	3.005	3.002
Ti	0.001	0.002	0.000	0.002	0.001	0.001	0.002	0.001	0.001	0.000	0.000	0.002
Al	2.002	2.011	1.991	1.988	2.005	2.007	1.996	1.997	1.999	2.008	2.002	2.009
Fe²⁺	2.167	2.277	1.935	2.006	2.105	2.164	2.039	2.238	2.226	2.310	1.850	2.044
Mg	0.718	0.565	0.837	0.771	0.622	0.519	0.751	0.515	0.654	0.562	0.973	0.760
Mn	0.049	0.074	0.072	0.085	0.095	0.138	0.036	0.062	0.026	0.027	0.015	0.021
Ca	0.060	0.064	0.125	0.097	0.170	0.163	0.164	0.160	0.073	0.072	0.146	0.147
X_{Fe}	0.75	0.80	0.70	0.72	0.77	0.81	0.73	0.81	0.77	0.80	0.66	0.73
X_{Alm}	0.72	0.76	0.65	0.68	0.70	0.73	0.68	0.75	0.75	0.78	0.62	0.69
X_{Sps}	0.02	0.02	0.02	0.03	0.03	0.05	0.01	0.02	0.01	0.01	0.01	0.01
X_{Prp}	0.24	0.19	0.28	0.26	0.21	0.17	0.25	0.17	0.22	0.19	0.33	0.26
X_{Grs}	0.02	0.02	0.04	0.03	0.06	0.05	0.05	0.05	0.02	0.02	0.05	0.05

Table 7.
Representative biotite SEM-EDS analyses.

Sample Setting	17-SS-8 Matrix	14-CH-9a Matrix	17-SS-17 Matrix	SC13-7 Matrix	SW13-2 Matrix	14-RG-01b Matrix
SiO₂	36.14	37.31	35.79	35.9	36.71	36.87
TiO₂	2.26	2.96	4.59	3.46	3.35	4.60
Al₂O₃	19.2	18.04	18.49	18.54	19.11	16.89
FeO	17.02	13.96	18.78	18.19	17.94	13.00
MgO	11.38	13.35	8.28	9.76	10.52	13.65
CaO	0.09	0.07	0.05	0.06	0.07	0.07
Na₂O	0.43	0.45	0.14	0.26	0.45	0.15
K₂O	9.02	9.13	9.77	9.36	9.51	9.79
Σ	95.54	95.27	95.89	95.53	97.66	95.02
Si	5.405	5.513	5.406	5.416	5.402	5.473
Ti	0.254	0.329	0.522	0.393	0.371	0.514
Al	3.385	3.142	3.292	3.296	3.314	2.955
Fe²⁺	2.129	1.725	2.372	2.295	2.208	1.614
Mg	2.537	2.941	1.865	2.195	2.308	3.021
Ca	0.014	0.011	0.008	0.01	0.011	0.011
Na	0.125	0.129	0.041	0.076	0.128	0.043
K	1.721	1.721	1.883	1.801	1.785	1.854
X_{Fe}	0.46	0.37	0.56	0.51	0.49	0.35

in Mg and cores slightly depleted in Fe ($X_{Fe} = 0.77-0.78$) and enriched in Mg. In these garnets, there is no evidence of X_{Ca} zoning, with values consistently falling between 0.05-0.06. This is again consistent with diffusive re-equilibration during resorption. However, one garnet within the sample is significantly different, yielding a slightly zoned core: rims yield a composition of $X_{Fe} = 0.81-0.82$, the outer core/inner rim yields $X_{Fe} = 0.78-0.79$, and the core yields $X_{Fe} = 0.82-0.83$. Additionally, this garnet exhibits strong Ca and Mn zoning: rims yield $X_{Ca} = 0.06$ and $X_{Sps} = 0.06$ and cores with $X_{Ca} = 0.19-0.21$ and $X_{Sps} = 0.18$. The composition of biotite grains in the matrix of the sample is $X_{Fe} = 0.56$, however the composition of biotite inclusions in garnet are depleted in Fe and range from $X_{Fe} = 0.37-0.50$. The

Table 8.
Representative SEM-EDS plagioclase analyses.

Sample	17-SS-8	17-SS-8	14-CH-9a	17-SS-17	17-SS-17	SC13-7	14-RG-01b
Mineral	Pl	Pl	Pl	Pl	Ksp	Pl	Pl
Setting	Grt Inclusion	Matrix	Matrix	Matrix	Matrix	Matrix	Matrix
SiO ₂	68.69	64.16	62.23	59.16	64.97	57.04	58.53
Al ₂ O ₃	19.59	22.65	23.5	25.54	18.73	27.00	25.51
FeO	0.08	0.06	0.00	0.01		0.03	0.01
CaO	0.07	3.3	5.11	7.34	0.17	8.99	7.46
Na ₂ O	12.57	10.58	9.18	7.82	0.95	6.73	7.64
K ₂ O	0.15	0.2	0.23	0.28	15.95	0.28	0.31
Σ	101.15	100.95	100.25	100.15	100.77	100.07	99.46
Si	2.979	2.815	2.758	2.642	2.981	2.561	2.634
Al	1.001	1.171	1.227	1.345	1.013	1.429	1.357
Fe ²⁺	0.003	0.002	0.000	0.000		0.001	2.044
Ca	0.003	0.155	0.243	0.351	0.008	0.432	0.361
Na	1.057	0.900	0.789	0.677	0.085	0.586	0.669
K	0.008	0.011	0.013	0.016	0.934	0.016	0.018
X _{An}	0.00	0.15	0.23	0.34	0.01	0.42	0.34
X _{Ab}	0.99	0.84	0.76	0.65	0.08	0.57	0.64
X _{Or}	0.01	0.01	0.01	0.02	0.91	0.02	0.02

composition of plagioclase in the matrix ranges from X_{An} = 0.31-0.34, however the composition of plagioclase inclusions is slightly lower yielding a spread between 0.13-0.32. K-feldspar grains in the matrix of the sample have compositions of X_{Or} = 0.87-0.91, where X_{Or} = K / (Ca + Na + K).

7.4. Sample SC13-7

Garnet in sample SC13-7 is Alm_{0.65-0.77}Prp_{0.16-0.27}GrS_{0.05-0.07}Sps_{0.01-0.03}. Garnet cores are unzoned in all porphyroblasts; however, the three analyzed grains yield slightly different core compositions possibly indicating various garnet populations. Each garnet yielded core values of X_{Fe} = 0.70-72, X_{Fe} =

0.77, and $X_{\text{Fe}} = 0.73$, with corresponding rim values of $X_{\text{Fe}} = 0.81-0.82$, $X_{\text{Fe}} = 0.80-0.83$, and $X_{\text{Fe}} = 0.81-0.87$, respectively. While not remarkably different, noticeable variation still exists, yet all rims are slightly enriched in Fe^{2+} and depleted in Mg suggesting diffusive re-equilibration during resorption. The composition of biotite inclusions in garnet is $X_{\text{Fe}} = 0.36-0.42$, which is slightly lower than that of the paleosome and neosome which are $X_{\text{Fe}} = 0.51-0.53$ and $X_{\text{Fe}} = 0.44-0.48$, respectively. Plagioclase was identified as inclusions within garnet in one grain, and yielded $X_{\text{An}} = 0.42-0.43$. Plagioclase in the matrix exhibited similar compositions also of $X_{\text{An}} = 0.42-0.43$. K-felspar in this sample exhibited strong exsolution, preventing discrete X_{Or} analyses to be obtained. The composition of cordierite rims around garnet ranges from $X_{\text{Fe}} = 0.33-0.34$, however inclusions of cordierite in garnet are slightly depleted in iron yielding values of $X_{\text{Fe}} = 0.29-0.31$.

7.5. Sample SW13-2

Garnet in sample SW13-2 is $\text{Alm}_{0.74-0.78}\text{Prp}_{0.18-0.22}\text{Grs}_{0.02-0.03}\text{Sps}_{0.01}$. Garnet cores are unzoned with $X_{\text{Fe}} = 0.77-0.78$ and $X_{\text{Ca}} = 0.02-0.03$. Rims are slightly enriched in Fe^{2+} and depleted in Mg yielding a composition of $X_{\text{Fe}} = 0.79-0.81$. Fe-Mg in the narrow rims is consistent with diffusive re-equilibration during resorption. The composition of biotite inclusions in garnet is $X_{\text{Fe}} = 0.41-0.47$, which is slightly lower than that of the matrix which yields $X_{\text{Fe}} = 0.48-0.50$. Plagioclase was not present in this sample.

7.6. Sample 14-RG-01b

Garnet in sample 14-RG-01b is $\text{Alm}_{0.62-0.69}\text{Prp}_{0.25-0.33}\text{Grs}_{0.04-0.05}\text{Sps}_{0.00-0.01}$. Garnet cores are unzoned with $X_{\text{Fe}} = 0.66-0.68$ and $X_{\text{Ca}} = 0.04-0.05$. Rims are slightly enriched in Fe^{2+} and depleted in Mg yielding a composition of $X_{\text{Fe}} = 0.72-0.73$. Fe-Mg in the narrow rims is consistent with diffusive re-

equilibration during resorption. The composition of biotite inclusions in garnet yields $X_{\text{Fe}} = 0.23-0.30$, whereas matrix grains exhibit higher compositional values of $X_{\text{Fe}} = 0.35-0.39$. Plagioclase in garnet and plagioclase in the matrix yielded similar compositional values, with inclusions yielding $X_{\text{An}} = 0.35-0.38$ and matrix grains yielding $X_{\text{An}} = 0.34-0.36$. The composition of cordierite rims around garnet ranges from $X_{\text{Fe}} = 0.19-0.20$, however inclusions of cordierite in garnet yield slightly more depleted values of $X_{\text{Fe}} = 0.17-0.19$.

Table 9.
Representative SEM-EDS cordierite analyses.

Sample Setting	SC13-7 Matrix	14-RG-01b Matrix
SiO₂	48.37	48.60
Al₂O₃	32.44	32.91
FeO	7.41	4.67
MgO	8.41	10.37
MnO	0.07	0.03
CaO	0.04	0.06
Na₂O	0.2	0.10
Σ	96.94	96.74
Si	5.029	4.999
Al	3.975	3.989
Fe²⁺	0.644	0.402
Mg	1.303	1.590
Mn	0.006	0.002
Ca	0.004	0.007
Na	0.04	0.02
X_{Fe}	0.33	0.2

8. Phase equilibria modeling

8.1. Sample 17-SS-8

In this sample, the peak assemblage of garnet + sillimanite + biotite + plagioclase + melt occurs

over a broad range range from 5.7-9.2 kbar and 715-800 °C (Figure 17). Calculated garnet isopleths of X_{Fe} in this field are consistent with observed core values of $X_{Fe} = 0.74-0.75$, while garnet isopleths of X_{Ca} are more broadly consistent with observed core values of $X_{Ca} = 0.02-0.04$. Predicted X_{Ca} values for plagioclase (0.19-0.31), however, are significantly lower than the observed values of $X_{Ca} = 0.13-0.15$.

Based on the observed assemblages and compositions of minerals that preserve their peak conditions, the area bounded by $X_{Fe(g)} = 0.74-0.76$ and $X_{Ca(g)} = 0.03-0.04$ refines peak $P-T$ conditions to 6.3-8.8 kbar and 728-760 °C.

The absence of cordierite in the sample aids in constraining the minimum pressure for retrograde conditions, which therefore cannot feasibly fall below ~5 kbar. Compositional values of X_{Fe} in garnet rims ($X_{Fe(g)} = 0.79-0.80$) aid in constraining the retrograde path conditions to approximately 5-6.7 kbar and 648-679 °C. However, measured compositions of X_{Fe} in biotite are much lower than predicted values along the retrograde path (0.46 vs 0.49-0.51) and therefore cannot help to refine retrograde $P-T$ conditions.

Mode isopleths indicate that melt is temperature sensitive throughout the entirety of the pseudosection, however garnet mode isopleths exhibit temperature sensitivity in the peak field but are pressure sensitive along the retrograde path. Regardless, from the peak assemblage along the retrograde path, garnet decreases from approximately 6 to 3 mol% and melt decreases from ~11 to 0 mol%. These results are consistent with petrographic observations of strongly resorbed garnet rims and the presence of melt pods composed of plagioclase and quartz. These results are suggestive of a clockwise $P-T$ path with peak conditions of 5.7-9 kbar and 730-760 °C followed by cooling and decompression to ~5-6.7 kbar and 650-680 °C.

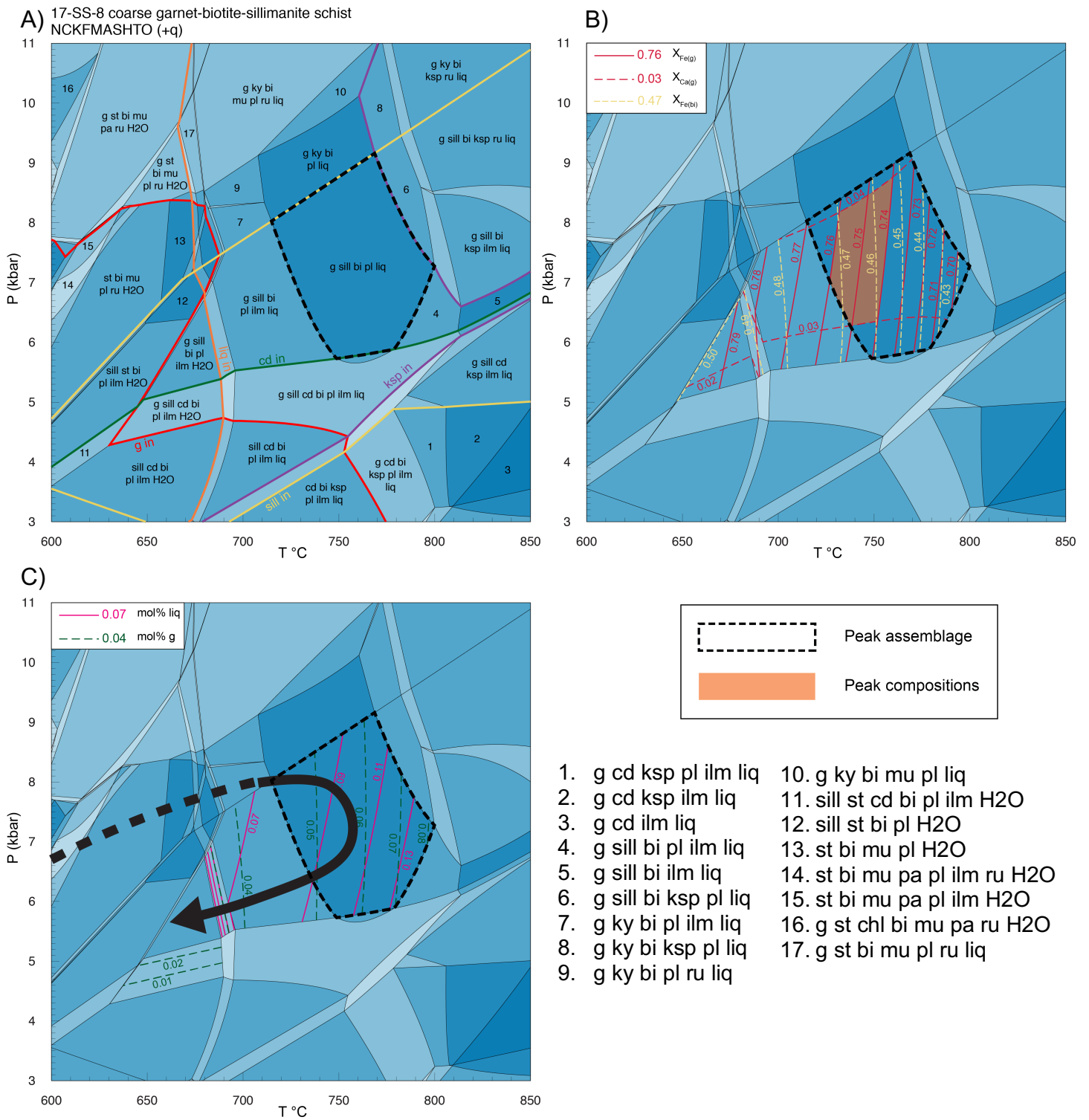


Figure 17. Pseudosection for sample 17-SS-8. **A)** Labeled assemblage fields with peak assemblage outlined and g, cd, sill, ksp, and liq-in lines highlighted. **B)** Compositional isopleths of $X_{Fe(g)}$, $X_{Ca(g)}$, and $X_{Fe(bi)}$ with peak compositions highlighted in orange. **C)** Modal isopleths of garnet and liquid with inferred P - T path.

8.2. Sample 14-CH-9a

In this sample, the peak assemblage of garnet + sillimanite + biotite + plagioclase + ilmenite + melt occurs over a broad range of 6.8-8.8 kbar and 695-845 °C (Figure 18). In this sample, the cordierite out line is unusually high pressure, which is responsible for slightly higher peak temperature than has been observed in other samples. Calculated isopleths of $X_{Ca(g)}$ are broadly consistent with analyzed compositions of garnet cores ($X_{Ca(g)} = 0.03-0.04$), however the observed Fe-Mg composition of garnet ($X_{Fe} = 0.69-0.70$) is more Fe-rich than what is predicted in this field ($X_{Fe} = 0.54-0.70$). Inconsistency between calculated isopleths and observed values furthermore carry over into $X_{Ca(pl)}$, in which observed values ($X_{Ca} = 0.23-0.25$) are slightly lower than predicted isopleth values for the peak field ($X_{Ca} = 0.26-0.27$). From the area bound by $X_{Ca(g)} = 0.03-0.04$ field, peak metamorphic conditions can be slightly refined to 6.8-8.8 kbar and 697-842 °C.

Measured compositional values of X_{Fe} in garnet rims range from 0.70-0.74 and measured $X_{Fe(bi)}$ values range between 0.36-0.38. Both sets of values fall along a reasonable retrograde path, and constrain retrograde metamorphic conditions to approximately 5.3-8.2 kbar and 630-652 °C.

Mode isopleths for this sample indicate that melt is temperature sensitive and garnet modes are generally temperature sensitive except at lower pressures. From the peak field along the retrograde path, garnet decreases from approximately 9 to 5 mol% and melt decreases from 6 to 0 mol%. These predicted calculations are consistent with slightly resorbed garnet rims and bands of melt composed of quartz and plagioclase found throughout the sample. In summary, these results suggest a clockwise P - T path with peak conditions of 6.8-8.8 kbar and 695-840 °C followed by cooling and minor decompression to 5.3-8.2 kbar and 630-652 °C.

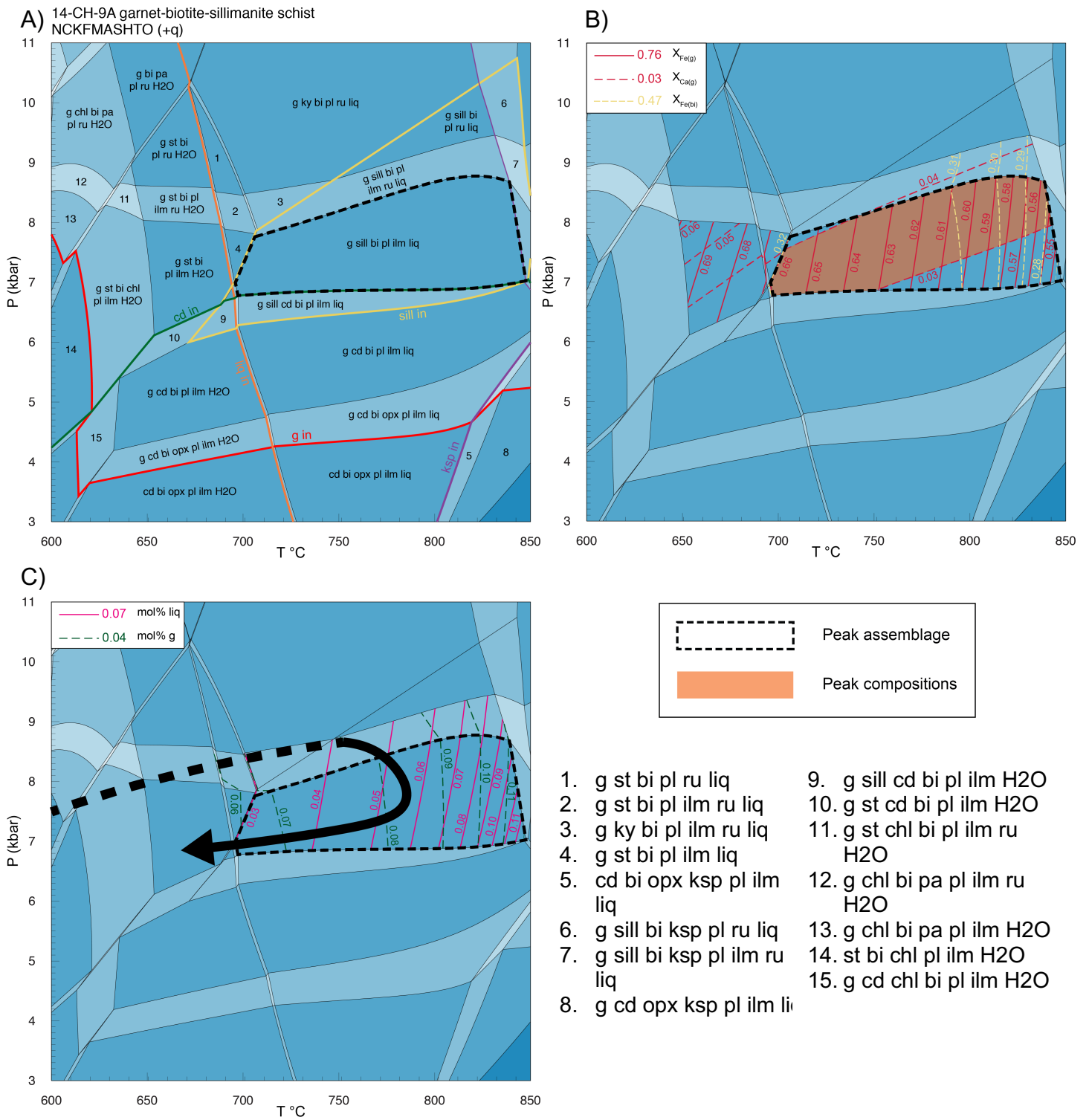


Figure 18. Pseudosection for sample 14-CH-9a. **A)** Labeled assemblage fields with peak assemblage outlined and g, cd, sill, ksp, and liq-in lines highlighted. **B)** Compositional isopleths of $X_{Fe(g)}$, $X_{Ca(g)}$, and $X_{Fe(bi)}$ with peak compositions highlighted in orange. **C)** Modal isopleths of garnet and liquid with inferred P - T path.

8.3. Sample 17-SS-17

In this sample, the peak assemblage of garnet + sillimanite + biotite + K-feldspar + plagioclase + ilmenite + melt occurs from 5.1-9 kbar and 745-775 °C (Figure 19). Calculated garnet isopleths of X_{Fe} in this field ($X_{Fe} = 0.76-0.80$) are consistent with measured core values of $X_{Fe} = 0.77-0.78$. Conversely, the observed value of X_{Ca} in garnet (0.06) is higher than the predicted isopleth values for the peak field ($X_{Ca(g)} = 0.02-0.05$). The composition of X_{Ca} in plagioclase behaves similarly, where calculated isopleth values (0.21-0.22) are significantly lower than measured compositional values of $X_{Ca(pl)} = 0.31-0.34$. Based on the observed assemblages and compositions of minerals that preserve their peak compositions, the area bound by $X_{Fe(g)} = 0.77-0.79$ marginally refine peak metamorphic conditions to 5.1-9 kbar and 752-772 °C.

Observed compositional values of both $X_{Fe(g)}$ and $X_{Fe(bi)}$ are lower than what would be expected for a traditional retrograde path according to predicted compositional isopleths for the sample. In this case, the measured compositions do not fall back below the solidus, making it difficult to deduce reasonable, precise constrains on retrograde metamorphic conditions. However, due to the lack of cordierite in the sample, the retrograde conditions most likely do not fall below ~4.5-5 kbar. Additionally, according to the pseudosection, retrograde temperatures would not reach above ~680 °C based on the position of the solidus.

Isopleths indicate that both mode of garnet and melt are temperature sensitive. From the peak assemblage field along the predicted retrograde path, garnet decreases from 12 to 3 mol% and melt decreases from 11 to 0 mol%. These results are consistent with resorbed garnet rims and the presence of melt layers. In summary, these results suggest a clockwise P - T path with peak conditions of ~5-9 kbar and 750-770 °C followed by cooling and decompression to conditions most likely around 5 kbar and 650 °C.

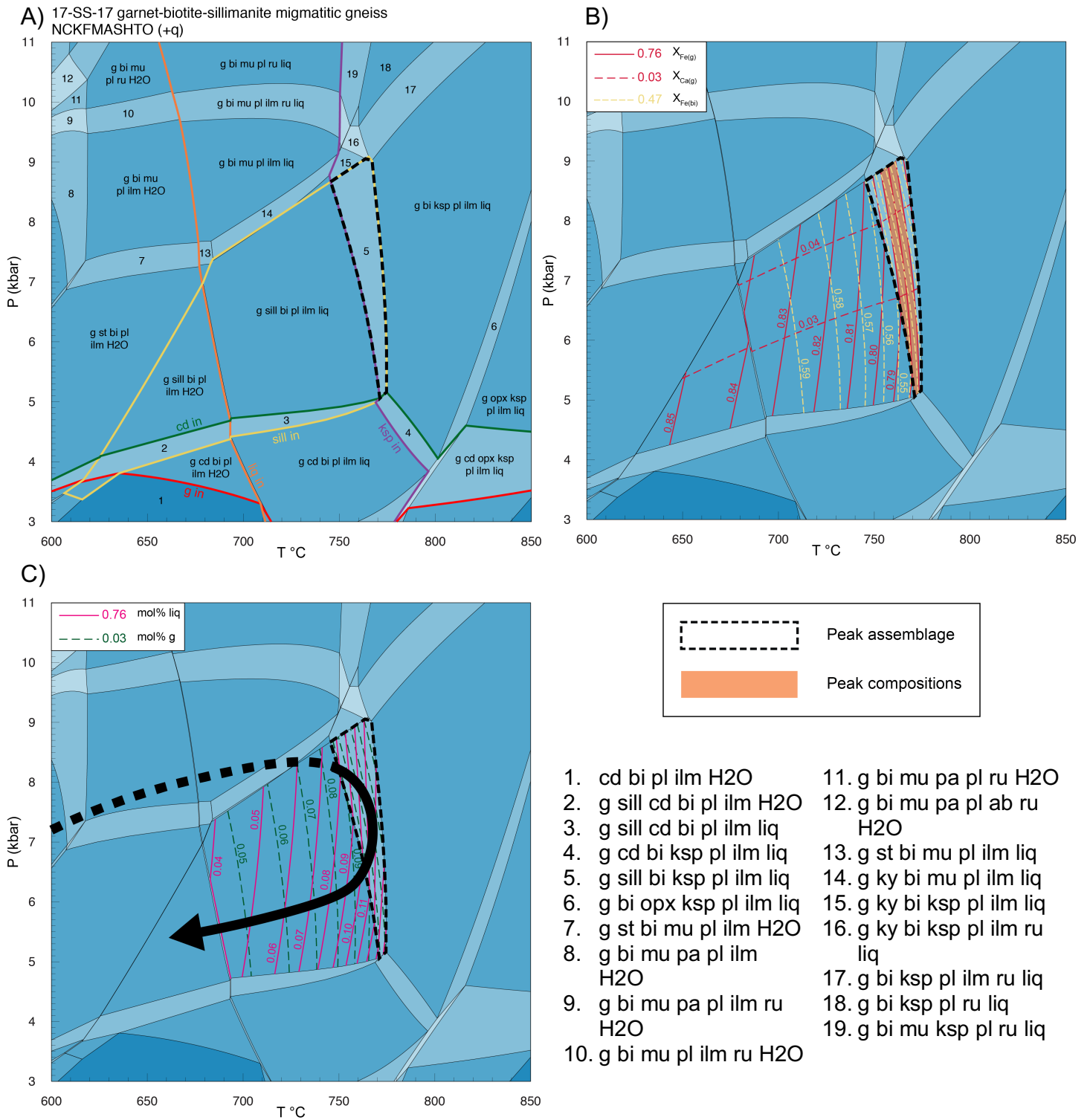


Figure 19. Pseudosection for sample 17-SS-17. **A)** Labeled assemblage fields with peak assemblage outlined and g, cd, sill, ksp, and liq-in lines highlighted. **B)** Compositional isopleths of $X_{Fe(g)}$, $X_{Ca(g)}$, and $X_{Fe(bi)}$ with peak compositions highlighted in orange. **C)** Modal isopleths of garnet and liquid with inferred P - T path.

8.4. Sample SC13-7

In this sample, the peak assemblage of garnet + sillimanite + biotite + plagioclase + rutile + melt occurs from 7.3-8.8 kbar and 702-832 °C (Figure 20). Calculated isopleths of $X_{Ca(g)}$ (0.05-0.08) are consistent with measured compositional values yielding $X_{Ca(g)} = 0.05-0.06$. $X_{Fe(g)}$ values for garnet cores range widely across various porphyroblasts, from approximately 0.70-0.77, which is reflective of multiple generations of garnet growth as proven by previously collected geochronology data. However, garnet with core values of $X_{Fe(g)} = 0.70-0.74$ are consistent with predicted isopleth values in the peak field (0.64-75). Plagioclase yields compositional values of $X_{Ca(pl)} = 0.42-0.43$ (with an average of 0.43) for both the matrix and garnet inclusions, which is also consistent with calculated isopleth values ($X_{Ca(pl)} = 0.42-0.45$). Based on observed assemblages and compositions of minerals that preserve their peak $P-T$ compositions, the area bound by $X_{Fe(g)} = 0.70-0.74$ and $X_{Ca(g)} = 0.06-0.07$ refine the peak $P-T$ conditions to 7.3-8.7 kbar and 702-780 °C.

Measured compositional values of X_{Fe} in garnet rims range from 0.80-0.83 and measured values of $X_{Fe(bi)}$ yield values between 0.51-0.53. These results constrain retrograde metamorphic conditions to ~4.3-5.4 kbar and 628-710 °C. This path is consistent with observed petrographic textures, most notably cordierite rims around garnet.

Mode isopleths indicate that melt is temperature sensitive. Mode of garnet also exhibits temperature sensitivity except for along the retrograde path which exhibits pressure sensitivity. From the peak assemblage field along the retrograde path, melt decreases from 7 to 0 mol% and garnet decreases from 8 to 1 mol%. These predicted calculations are consistent with petrographic observations of resorbed garnet rims and compositional bands of melt present within the sample. Additionally, mode isopleths of cordierite exhibit pressure sensitivity indicating growth during decompression and increase from 0 to ~5 mol% along the retrograde path. In summary, these results suggest a clockwise $P-T$ path,

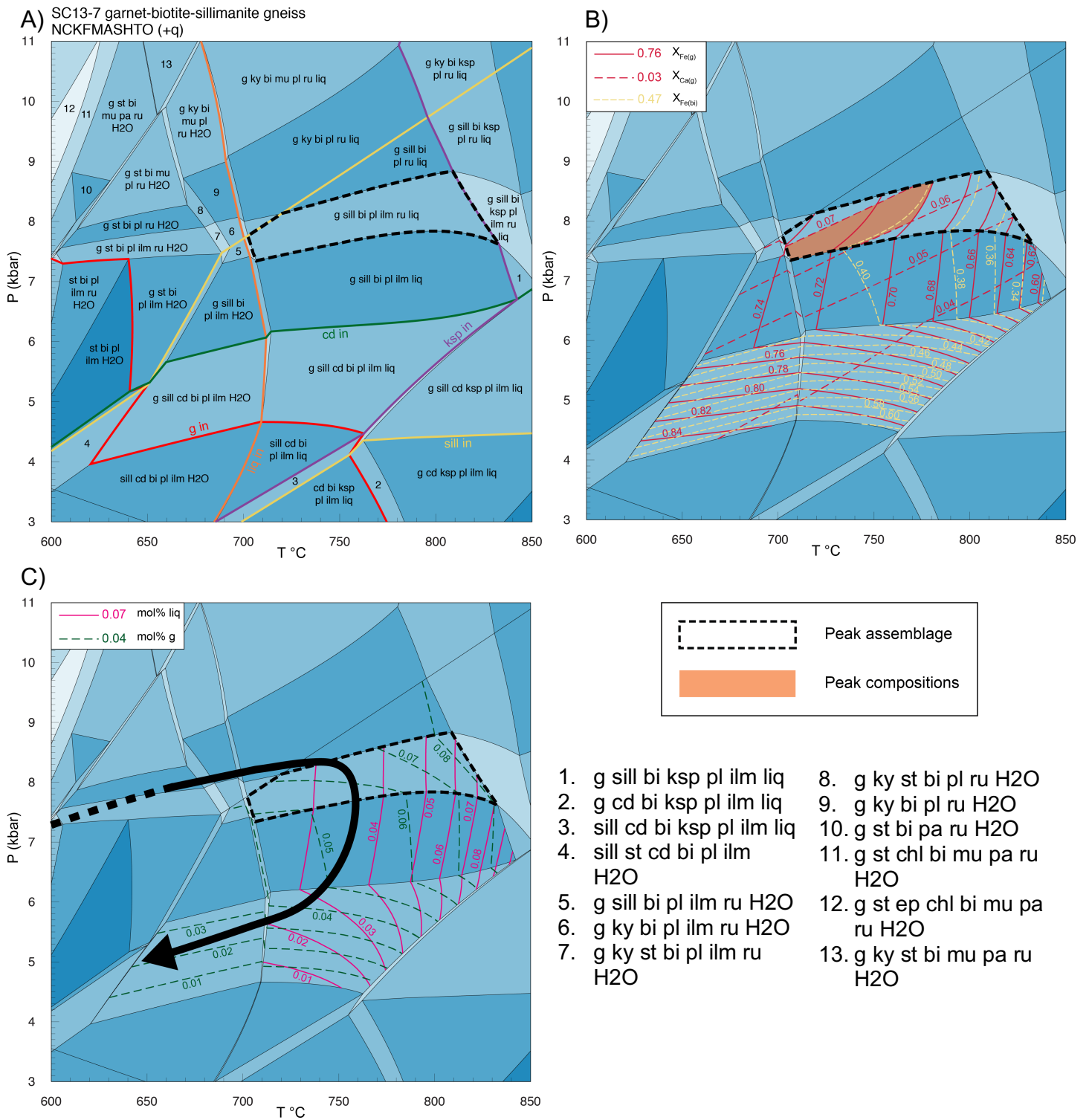


Figure 20. Pseudosection for sample SC13-7. **A)** Labeled assemblage fields with peak assemblage outlined and g, cd, sill, ksp, and liq-in lines highlighted. **B)** Compositional isopleths of $X_{Fe(g)}$, $X_{Ca(g)}$, and $X_{Fe(bi)}$ with peak compositions highlighted in orange. **C)** Modal isopleths of garnet and liquid with inferred P - T path.

with peak P - T conditions of ~ 7.3 - 8.7 kbar and 700 - 780 °C followed by decompression and cooling to ~ 4.3 - 5.4 kbar and 630 - 710 °C.

8.5. Sample SW13-2

In this sample, the peak assemblage of garnet + sillimanite + biotite + ilmenite + rutile + H₂O + melt occurs from 6.1 - 9.2 kbar and 709 - 767 °C (Figure 21). For this sample, the H₂O value was chosen in order to fully saturate the subsolidus portion of the diagram using the lowest possible value, however an unusual widening of the region between the solidus and liquidus occurred between ~ 6.1 - 9.5 kbar. Calculated garnet isopleths of X_{Fe} in this field (0.77 - 0.80) are broadly consistent with observed garnet core values yielding X_{Fe(g)} = 0.77 - 0.78 . Alternatively, calculated garnet isopleths of X_{Ca} in the peak field (0.09 - 0.11) are significantly higher than observed X_{Ca} values of garnet cores (0.02 - 0.03). Based on these observations, the area bound by X_{Fe(g)} = 0.77 - 0.79 refines peak P - T conditions to 6.2 - 8.9 kbar and 730 - 762 °C.

Measured compositional values of X_{Fe} in garnet rims yield values between 0.79 - 0.81 which is consistent with predicted isopleth values along the retrograde path. Measured values of X_{Fe} in biotite, however, yield values between 0.48 - 0.50 which is slightly lower than values predicted along the retrograde path in the pseudosection (0.50). Due to these inconsistencies, limitations on retrograde conditions can only be confidently placed on temperature estimates yielding a range between 650 - 730 °C. Only a minimum pressure for the retrograde path can be deduced from the diagram based on the lack of cordierite in the sample, which infers that conditions did not fall below ~ 4.5 kbar.

Mode isopleths indicate that melt is temperature sensitive. Alternatively, garnet is primarily temperature sensitive above the solidus yet below the solidus garnet growth is pressure sensitive. From the peak assemblage field along the retrograde path, melt decreases from 2 to 0 mol% and garnet

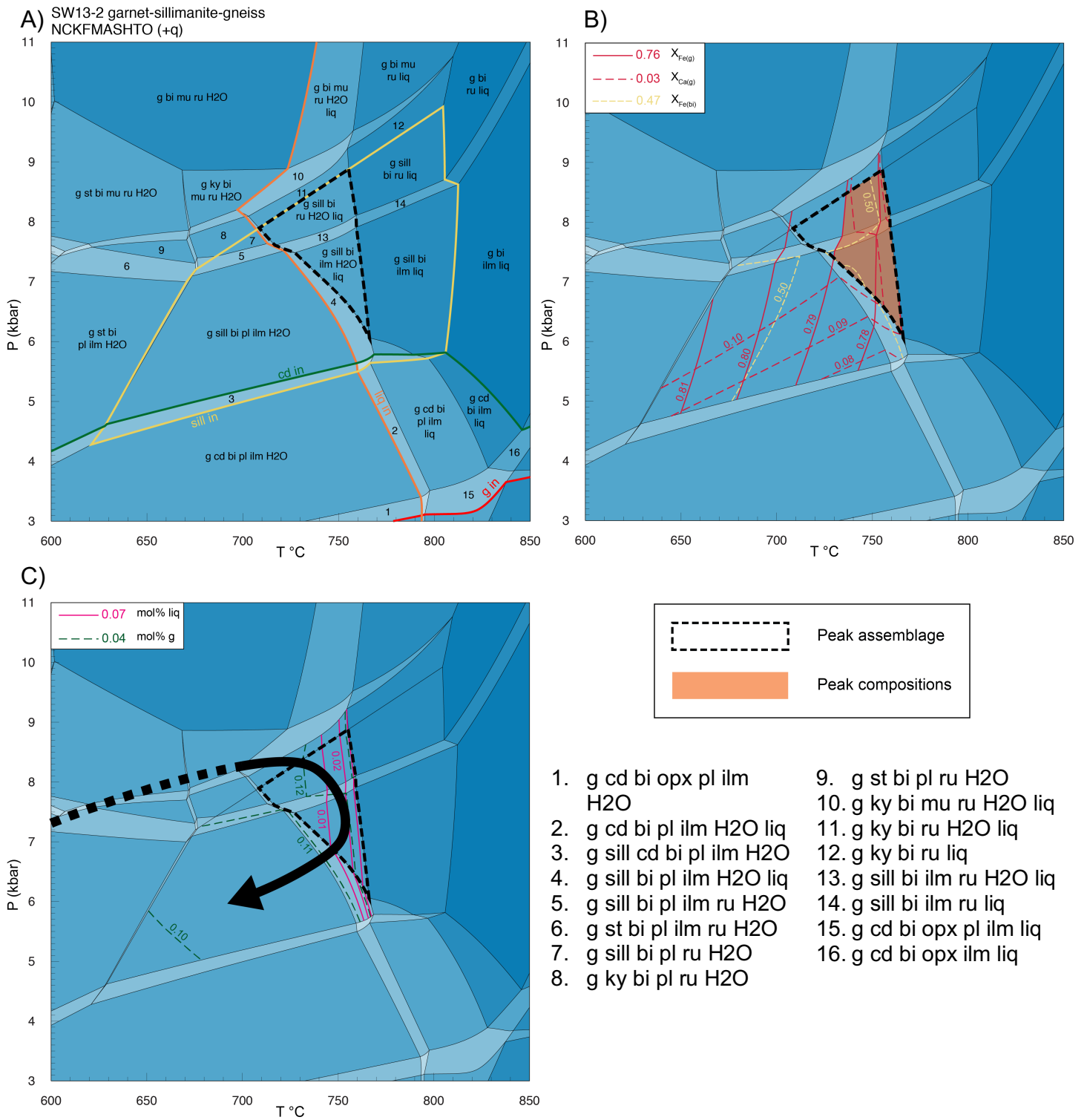


Figure 21. Pseudosection for sample SW13-2. **A)** Labeled assemblage fields with peak assemblage outlined and g, cd, sill, ksp, and liq-in lines highlighted. **B)** Compositional isopleths of $X_{Fe(g)}$, $X_{Ca(g)}$, and $X_{Fe(bi)}$ with peak compositions highlighted in orange. **C)** Modal isopleths of garnet and liquid with inferred P - T path.

decreases from 12 to 10 mol%. These modes are consistent with observations in the sample, considering the presence of little to no melt within the rock and only mildly altered garnet rims. Regardless, these observations are suggestive of a clockwise P - T path with peak conditions of 6-9 kbar and 730-760 °C followed by decompression and cooling to ~4.5 kbar and 650-730 °C.

8.6. Sample 14-RG-01b

In this sample, the peak assemblage of garnet + sillimanite + biotite + plagioclase + rutile + melt occurs from 7.4-10 kbar and 712-808 °C (Figure 22). Calculated garnet isopleths of X_{Ca} in this field ($X_{Ca(g)} = 0.04$ - 0.07) are consistent with observed core values of $X_{Ca} = 0.05$, while predicted garnet isopleths of X_{Fe} (0.54-0.57) are notably lower than observed core values which yield $X_{Fe(g)} = 0.66$ - 0.68 . Conversely, observed X_{Ca} values of plagioclase are considerably lower than calculated isopleths for the field (0.35-0.36 vs. 0.41-0.44). Based on the observed assemblages and compositions of minerals that preserve their peak conditions, the area bound by $X_{Ca(g)} = 0.05$ - 0.06 refines peak P - T conditions to 7.5-9.4 kbar and 712-808 °C.

Measured compositional values of X_{Fe} in garnet rims range from 0.72-0.73 and measured values of $X_{Fe(bi)}$ yield values between 0.35-0.39. These results constrain retrograde conditions to approximately 5.8-6.7 kbar and 662-710 °C. These constraints indicate the presence of cordierite along the retrograde path which reflects observed textures of cordierite rims around garnet.

Mode isopleths indicate that melt is temperature sensitive. However, garnet is temperature sensitive above ~7.5 kbar and pressure sensitive below ~7.5 kbar. From the peak assemblage field along the retrograde path melt decreases from 8 to 0 mol% and garnet decreases from ~12 to 2 mol%. This is consistent with petrographic observations of highly resorbed garnet rims and large amount of plagioclase feldspar indicating substantial melting. Additionally, cordierite increases from 0 to

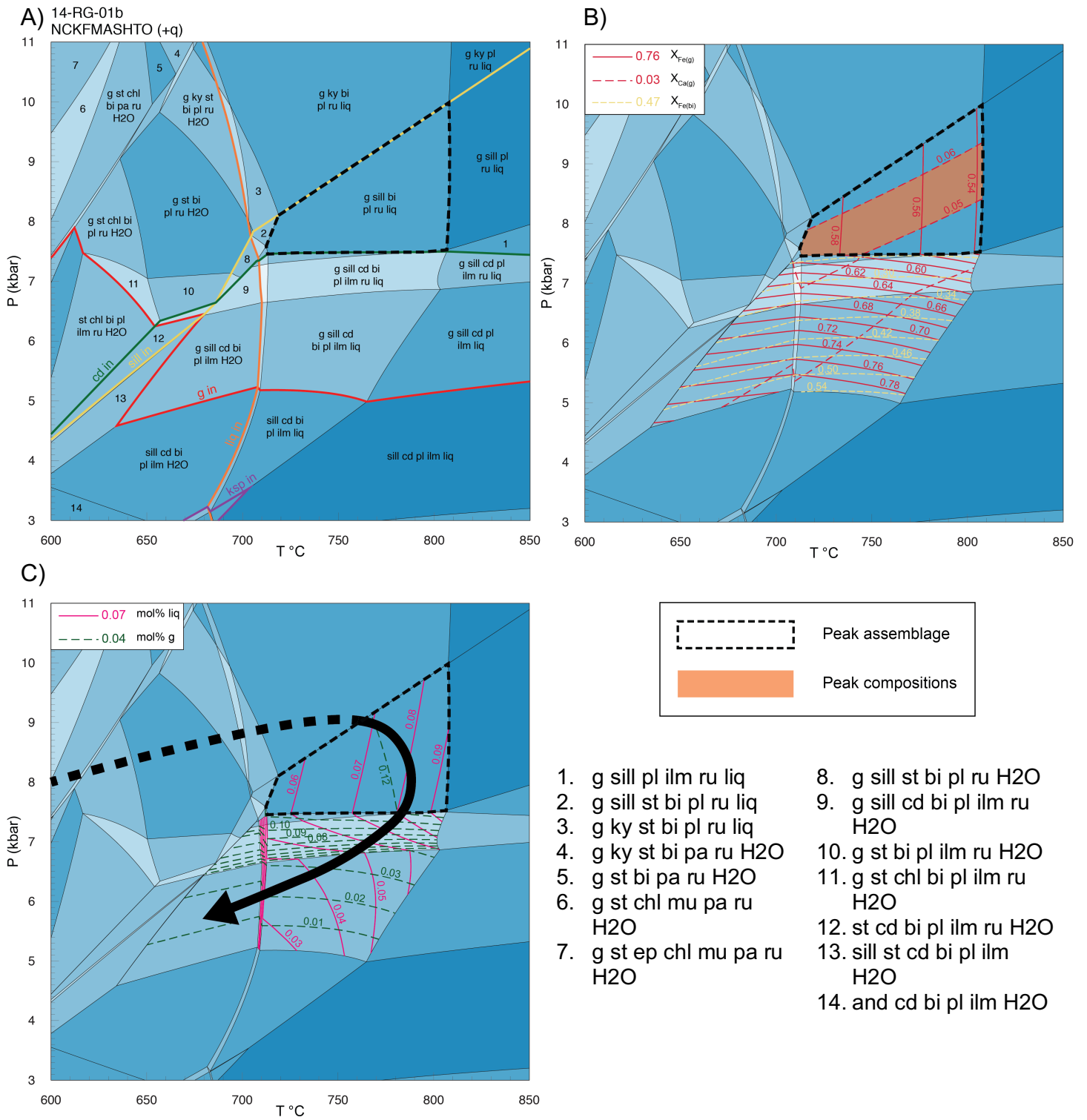


Figure 22. Pseudosection for sample 14-RG-01b. **A)** Labeled assemblage fields with peak assemblage outlined and g, cd, sill, ksp, and liq-in lines highlighted. **B)** Compositional isopleths of $X_{Fe(g)}$, $X_{Ca(g)}$, and $X_{Fe(bi)}$ with peak compositions highlighted in orange. **C)** Modal isopleths of garnet and liquid with inferred P - T path.

approximately 10 mol%, which is consistent with the presence of cordierite rims around garnet. These results therefore suggest a clockwise P - T path with peak conditions of 7.5-9.4 kbar and 712-808 °C.

9. Discussion

9.1. P - T Paths

Phase equilibria modeling suggest that all six samples were metamorphosed to upper amphibolite facies conditions. All samples reached suprasolidus conditions except for SW13-2 from the EGS in the southwestern portion of the Mine Gulch quadrangle.

Pelitic schists from the CRMS (17-SS-8, 14-CH-9a, 17-SS-17) all reached suprasolidus conditions with temperatures and pressures exceeding 700 °C and 7 kbar. Peak temperatures were well preserved in sample 17-SS-17, however modeling did not provide robust constraints for peak pressures due to the modification of Fe-Mg compositions during retrograde re-equilibration. Furthermore, peak conditions modeled in sample 14-CH-9a were too broad (6.8-8.8 kbar, 697-842 °C) to aid in placing effective constraints on peak metamorphic conditions for the sample. This is because peak conditions in 14-CH-9a were constrained solely by X_{Ca} concentrations in garnet cores, which must be approached with caution. Although Ca concentrations in garnet cores for this sample plot within the inferred peak assemblage Ca disequilibrium during garnet growth has been documented (e.g. Spear and Daniel, 2001) and re-equilibration during retrograde metamorphism can yield atypical results (Carlson, 2006; Caddick et al., 2010).

Regardless, peak metamorphic phases were well preserved in samples 17-SS-8 and 17-SS-17 from the CRMS. Sample 17-SS-8 was collected from near the structural top of the CRMS, whereas sample 17-SS-17 was collected from the base of the suite, however both produced similar predictions for peak metamorphic pressures (5.7-9 kbar and 5-9 kbar, respectively). On the other hand, temperature

predictions from the two samples show that sample 17-SS-8 produced slightly lower peak temperatures (730-760 °C) than sample 17-SS-17 (750-770 °C). A pelite from the middle CRMS modeled by Cramer (2015), structurally in-between 17-SS-8 and 17-SS-17, yielded similar peak metamorphic conditions of 5.7-7.1 kbar and 760-770 °C. Furthermore, Berg (2015) conducted geothermometry on a series of amphibolites from the upper portion of the CRMS which, from structurally highest to structurally lowest, produced results which range between 700 ± 80 °C, 7.4 ± 1.4 and kbar 740 ± 80 °C and 7.5 ± 1.4 kbar. These comparisons across a variety of studies show that while peak pressure conditions throughout the CRMS during the Big Sky orogeny remained reasonably constant, peak metamorphic temperatures increase towards lower structural levels within the suite.

Peak metamorphic conditions for a leucosome-rich layer from pelitic migmatite 14-RG-01b located in the Dillon Gneiss, immediately structurally below the CRMS, is inferred at 712-808 °C and 7.4-9.4 kbar. These constraints, however, are broad and directly affected by Fe-Mg re-equilibration during retrograde metamorphism. Similar to sample 14-CH-9a from the CRMS, peak conditions are constrained solely by X_{Ca} concentrations in garnet cores which have the likelihood of producing erratic results. Decompression is constrained texturally by the presence of cordierite rims around garnet in addition to matrix biotite X_{Fe} compositions, yielding conditions which fall between ~5.8-6.7 kbar and 662-710 °C. Presently, no other studies have estimated P - T conditions from any lithologies within the Dillon Gneiss. Nonetheless, this result broadly suggests that at least the TOR locality in the Dillon Gneiss experienced lower peak metamorphic pressures than the CRMS. Peak temperature conditions from this sample are too broad (712-808 °C) to draw confident comparisons to estimates from the CRMS, however it does fall within the same margin of error as samples from the suite.

Pelitic schist SW13-2 from the EGS located in the southwestern portion of the study area lacked evidence of melt in thin section based on the absence of feldspar (either plagioclase or K-feldspar).

However, this does not necessarily mean that the rock did not reach suprasolidus conditions: either leucosome wasn't preserved, or, because the bulk rock geochemistry for this sample was taken from its thin section, it is possible the portion of rock the thin section was cut from wasn't an entirely representative piece of the whole. Further issues that may have resulted from collecting the bulk chemistry from the sample's thin section include an issue with the solidus in SW13-2. In this sample, the solidus appears to have been shifted up temperature considerably in comparison to SC13-7, also from the EGS. Furthermore, there is a considerably large gap between the solidus and liquidus between ~6-9 kbar which could not be corrected for by lowering the H₂O value without losing water saturation along the extent of the solidus. Another circumstance to consider with regards to modeling this sample was that the bulk geochemistry results showed a complete lack of Na₂O which is unusual for pelitic rocks of this nature. In order to model the pseudosection, we assumed that there was at least 0.01% of Na₂O in the sample, however that is still a very small amount. It is also possible that this wasn't an issue associated with the sample's bulk chemistry whatsoever: it could be that the sample has an unusual protolith that happens to be low in sodium. These caveats notwithstanding, measured X_{Fe} compositions of garnet cores and rims did fall in the peak predicted field, and modeling yielded peak metamorphic conditions of 6.2-8.9 kbar and 730-763 °C. Desmarais (1981) conducted geothermometry from a sample of meta-ultramafic rock near where SW13-2 was collected, and determined peak conditions of ~710 °C and 5-7 kbar.

For sample SC13-7 from the EGS located just off the eastern edge of the study area, peak metamorphism is inferred at 7.3-8.7 kbar and 700-780 °C. Intergrain Fe-Mg variation observed in this sample is likely the result of garnet nucleation and growth along the prograde path at different points in time; garnets forming earlier would have higher X_{Fe} values than those forming at a later time. Peak metamorphic conditions for this sample are relatively well constrained by X_{Fe} and X_{Ca} garnet core

values, which means that Fe-Mg compositions have not been as seriously affected by retrograde re-equilibration in comparison to other samples from this study. Decompression is constrained by the presence of cordierite rims around garnet in addition to X_{Fe} values of biotite in the matrix yielding constrains between $\sim 4.3\text{-}5.4$ kbar and $628\text{-}710$ °C. An amphibolite sample from Berg (2015) in the EGS collected ~ 0.2 miles away from SC13-7 yielded somewhat similar peak metamorphic conditions of 7.4 ± 1.4 kbar and 780 ± 100 °C.

Additional P - T estimates from the EGS were calculated by Cramer (2015) from two supplementary localities within the Ruby Range. Two samples are from the Elk Gulch area, located in the southern portion of the Ruby Range, which yielded peak conditions of $\sim 8.1\text{-}9$ kbar, $770\text{-}800$ °C and $\sim 8\text{-}11$ kbar and $710\text{-}770$ °C. The remaining two samples are from the Sweetwater Creek area, which is located along the southeastern edge of the Ruby Range, and yielded peak conditions of $7.7\text{-}9.7$ kbar, $710\text{-}830$ °C and $7.8\text{-}9.1$ kbar, $740\text{-}830$ °C. While predictions of peak metamorphic temperatures from the EGS are broad and vary across different localities throughout the range, it can be determined that the EGS experienced higher peak temperatures and pressures than both the CRMS and DG.

In summary, it appears that there is some variety in peak metamorphic conditions between and within the three major structural units within the Ruby Range. In the CRMS, all predicted peak pressure conditions were generally similar, averaging ~ 7 kbar. However, there is a noticeable increase in temperature from the top towards the base of the CRMS: predicted peak temperatures increase from ~ 700 °C to ~ 760 °C. The only sample which predicts peak conditions from the Dillon Gneiss comes from this study, which yielded conditions of ~ 760 °C and ~ 8.4 kbar. The predicted temperature value is similar to that of the lower CRMS, however the pressure estimate is considerably higher. The structurally lowest major unit within the range, the EGS, can be considered in terms of the four separate localities as described above. The area in the southwestern corner of the Mine Gulch quadrangle where

SW13-2 was collected produced average P - T conditions of ~ 6.8 kbar and ~ 735 °C, the region where SC13-7 was collected averaged peak conditions of ~ 7.7 kbar and ~ 760 °C, the Elk Gulch locality averaged ~ 9 kbar and ~ 762 °C, and the Sweetwater Creek locality averaged ~ 8.6 kbar and ~ 778 °C. While there is some variability in these results, it appears that samples from the EGS in the northern portion of the Ruby Range yield lower P - T results than those found in the southern portion of the range. Additionally, it is evident that the EGS exhibits the highest P - T estimates from the range in comparison to the CRMS and Dillon Gneiss. This infers that the rocks in this region are the structurally deepest out of all units within the Ruby Range.

9.2. P - T - t Paths

Sample 14-RG-01b from the QFG, SC13-7 from the EGS, and 14-CH-9a from the CRMS have corresponding U-Pb monazite ages which were collected as part of an internal grant from Amherst College awarded to Tekla Harms. This information was received via personal communication with Tekla Harms in May 2017 for U-Pb geochronological data obtained from the University of California – Santa Barbara (UCSB) laser ablation split stream Petrochronology Lab. These new ages aid in constraining the timing of peak metamorphism in conjunction with their respective pseudosections for each major unit in the region. The data discussed here is consistent with previously collected geochronology data in the region: monazite preserved U-Pb dates for both the ~ 2.45 Ga Tendoy orogeny in addition to the ~ 1.78 Ga Big Sky orogeny. However, only the Big Sky ages are applicable to constraining P - T - t paths for each pseudosection given that relict Tendoy conditions were not preserved. Because of this, the ~ 1.78 - 1.72 Ga ages will be the focus of this section.

Monazite in sample 14-RG-01b from the DG yielded two distinct age populations with weighted mean ages of 2438 ± 4 Ma (Tendoy) and 1775 ± 9 Ma (Big Sky). While predictions for peak

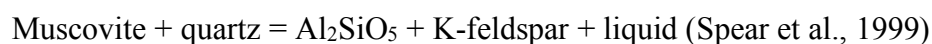
metamorphic conditions from this sample are broad (712-808 °C and 7.4-9.4 kbar), the timing of peak metamorphism in this sample is nevertheless consistent with ~1.78-1.72 Ga ages from previous studies (Jones, 2008; Cramer, 2015). Monazite in sample SC13-7 from the EGS produced primarily ~1.78-1.72 Ga ages yielding a weighted mean age of 1759 ± 4 Ma with a handful of older, relict ~2.45 Ga ages. While the weighted mean of this sample is slightly younger than that of 14-RG-01b by approximately 15 million years, EGS samples from Cramer (2015) also yielded slightly younger ages which range between 1748-1769 Ma. Lastly, sample 14-CH-9a from the CRMS also produced primarily ~1.78-1.72 Ga ages, but also yielded a few older discordant ~2.45 Ga grains. However, the primary population yielded a weighted mean age of 1780 ± 5 Ma, which additionally agrees with published ages from Jones (2008) and Cramer (2015). In summary, it appears that both the Dillon Gneiss and CRMS reached peak metamorphic conditions at approximately the same time ca. 1.78 Ga, however the EGS did not reach peak conditions until ~15 million years later at ca. 1755 Ma.

This new geochronology data also has significant implications in regards to inferences made about the relationships between the major map units in the Ruby Range. When considered in conjunction with age data collected by Jones (2008) and Cramer (2015) (Table 1), it is evident that all three major units within the Ruby Range exhibit evidence of both the ~2.45 Ga and ~1.78-1.72 Ga events. This further supports the conclusions that these units are very closely structurally related and also share an entwined metamorphic history. However, the CRMS better preserves 1.78-1.72 Ga ages, and the EGS best preserves ca. 2.45 Ga ages (Jones, 2008; Cramer, 2015). Two additional samples which were dated at UCSB are now of particular interest to the story: sample 15-RR-55b which was collected from the garnet leucogneiss within the lower CRMS north of the Stone Creek fault, and sample 14-CH-13 which is a pelite also collected from the lower CRMS. Sample 15-RR-55b exhibits exclusively ~2.45 Ga ages, yielding a weighted mean age of 2479 ± 5 Ma. This is significant because the

MGL has only exhibited evidence of ~2.45 Ga ages with no evidence of younger ~1.78-1.72 Ga ages, although the unit intrudes into the DG, the EGS, and CRMS, which all reveal ages from both populations. This is also supported a Lu-Hf garnet age from a sample of garnet leucogneiss that intrudes into the base of the CRMS which yielded an age of 2428.1 ± 6.8 Ma (Baker et al., 2017). Similarly, sample 14-CH-13 yields a weighted mean age of 2440 ± 8 Ma, and is the only sample from the CRMS that exhibits entirely ~2.45 Ga ages with no evidence of ca. 1.78-1.72 Ga overprinting.

9.3. Implications for melt and lack of K-feldspar

The range of melt predicted in peak metamorphic fields across all samples falls between 0 and 14 mol%. This falls far below the critical melt fraction (CMF) of 30 vol%, inferring that all melt from the chosen sample locations were generated *in-situ* and did not experience melt loss to shallower crustal levels (Wickham, 1987). In all samples in which leucosome is observed, the melt composition is primarily tonalitic which is unusual for melt generated from average pelitic rocks. In the KASH (K_2O , Al_2O_3 , SiO_2 , H_2O) system, the primary melt producing reaction for a clockwise *P-T* path is:



While all samples from this study were modeled in the NCKFMASHTO system, the addition of remaining phases does not change the fact that K-feldspar is expected to be generated during most melt producing reactions (Spear et al., 1999). Nevertheless, the lack of muscovite observed in rocks from the Ruby Range is consistent with rocks undergoing muscovite dehydration melting. However, pelites from the CRMS, DG, and EGS are all very K-feldspar poor.

Regardless, all samples do exhibit evidence of compositional layering which is consistent with partial melting. Additionally, the mineral assemblage of observed leucosome is largely consistent with the expected composition of melt generated from a pelitic rock with the exception of alkali feldspar in

samples from the CRMS and DG. In order to reconcile the lack of K-feldspar with the predicted reaction from these two major units, there are two main scenarios to consider.

The first would be the primary injection of tonalitic melt from a nearby source into the metamorphic system. This is unlikely, however, because the textures of observed migmatites in the region are primarily schleiren in nature. If the migmatites formed through injection, one would expect to observe sharper edges around the injected leucosome (Pawley et al., 2013). Additionally, in particular regards to the CRMS pelites, cordierite and garnet are often present in the leucosome, albeit in small quantities, which most likely represent the solid products of the *in situ* melt reaction (Spear et al., 1999; Pawley et al., 2013). Therefore, it would be difficult to reconcile the formation of these minerals in an injected tonalitic melt. Also, as previously mentioned, the vol% of melt present in these rocks is also far below the CMF further supporting the idea that melt formed within the CRMS, DG, and EGS was generated *in situ*.

The second scenario is that potassium was removed from the system during anatexis. This would involve two distinct generations of melt production, which can be reconciled by the occurrence of the garnet leucogneiss. As previously discussed, the garnet leucogneiss is direct evidence of large-scale crustal melting which occurred at ca. 2.45 Ga based on recent monazite and garnet geochronology. This suggests that the unit formed as a result of melt segregation associated with collision and metamorphism during the Tendoy orogeny. The unit contains substantial amounts of K-feldspar in comparison to pelites from the CRMS, DG, and EGS, which infers that the pelite from which the melt was sourced from was rich in muscovite. This means that by ca. 1.78 Ga, muscovite was only found in small quantities throughout the Ruby Range because it was consumed ca. 2.45 Ga as a result of muscovite dehydration melting. This explains the tonalitic nature of melt observed within the remaining units in the region. Additionally, although biotite is found abundantly within pelites throughout the

range, temperatures during the Big Sky orogeny were not high enough to promote the dehydration melting of biotite which begins around ~900 °C. In summary, the Ruby Range experienced two major melt producing events, however the majority of potassium present in the range was consumed and segregated out ca. 2.45 Ga, which led the second generation of melt produced ca. 1.78 Ga to be tonalitic in nature.

10. Tectonic Interpretation

10.1. Early Proterozoic collisional orogenesis: The Tendoy Orogeny

~2.45 Ga metamorphic zircon and primarily monazite ages are relatively common within Tendoy Mountains, Beaverhead Mountains, Tobacco Root Mountains, and the Ruby Range (Dahl et al., 2002; Roberts et al., 2002a; Kellogg et al., 2003; Jones, 2008; Cramer, 2015). Roberts et al. (2002) first proposed that sediments of the MMT were deposited between ~2.75-2.57 Ga and suggested that the region experienced an early, “cryptic” ~2.47 Ga metamorphic event. The timeframe of this early event coincides temporally with a global superplume event, and at the time it was believed that these ages were possibly related to the break-up of the supercontinent Kenorland (Roberts et al., 2002a; Dahl et al., 2004). As more 2.45 Ga ages were identified in adjacent mountain ranges it became evident that early Paleoproterozoic metamorphism was widespread throughout the MMT and was more likely attributed to a local tectonothermal event. Kellogg et al. (2003) then suggested that ~2.45 Ga ages represent the age of granitic plutonism, metamorphism, and crustal consolidation. While an exact mechanism had not yet been proposed, these are all within the same timeframe of $^{40}\text{Ar}/^{39}\text{Ar}$ cooling ages from hornblende, muscovite, and biotite in the Madison mylonite zone (MMZ) (Erslev and Sutter, 1990).

The MMZ is located in the Southern Madison Range (SMR), which lies ~40 miles southeast of the Ruby Range, and is a 3-km-thick zone of northeast-trending, northwest-dipping reverse faults

(Erslev and Sutter, 1990). The MMZ is characterized by the rotation of foliations and layering from southeast to northwest dipping orientations, retrograde metamorphism of mafic rocks, and strong downdip stretching fabrics (Erslev and Sutter, 1990). The region encompasses the contact between basement gneisses and metasedimentary rock in the SMR, similar to the lithologies observed in the Ruby Range (Erslev and Sutter, 1990). In the SMR, the two units in question are the Cherry Creek Metamorphic Suite (CCMS) and pre-Cherry Creek Metamorphic Complex (PCCMC), which is synonymous with the original names given to the Christensen Ranch Metasedimentary Suite and the Elk Gulch Suite, respectively. The CCMS, similar to the CRMS, is a sequence of dolomitic marble, biotite-staurolite-garnet schist, quartzite, and amphibolite, and the PCCMS is comprised of basement granulites (Erslev and Sutter, 1990).

$^{40}\text{Ar}/^{39}\text{Ar}$ thermochronology conducted from a series of samples within the MMZ revealed a cooling age of 2.5 Ga for hornblende and muscovite and a cooling age of 2.4 Ga for biotite (Erslev and Sutter, 1990). These ages suggest a metamorphic maximum of approximately 2.75 Ga, which reasonably coincides within the same timeframe of observed 2.45 Ga ages from the Ruby Range and surrounding region (Erslev and Sutter, 1990). Erslev and Sutter suggested that the MMZ and associated ages are representative of a major compressional orogenic event which reworked a significant amount of Archean basement in southwest Montana (Erslev and Sutter, 1990). It is therefore reasonable to assume that the collisional event which led to the formation of the MMZ is temporally equivalent to the event responsible for producing 2.45 Ga ages in the Tendoy Mountains, Beaverhead Mountains, Tobacco Root Mountains, and the Ruby Range. Collectively, all of these data and associated rocks, textures, and assemblages are more consistent with regional metamorphism with the MMZ recording the suturing of the MMT to the margin of the Wyoming Province at that time (Figure 23). This would also imply that the MMT experienced two discrete cycles of sedimentation and deposition on the cratonic margin: one

between ~2.75-2.45 Ga before the Tendoy orogeny, and a second between ~2.45-1.8 Ga pre-Big Sky orogeny (Figure 23). This idea is supported by the identification of preserved ~2.45 Ga monazite ages from the lower portion of the CRMS in the Ruby Range.

10.2. Post 2.45 Ga extensional tectonism and dike/sill emplacement

Within the Precambrian rocks of the Tobacco Root Mountains, there are a number of tholeiitic metamorphosed mafic dikes and sills (MMDS) which cross-cut the gneissic banding of Archean gneisses (Mueller et al., 2004). Ion microprobe analyses on zircon from one dike of the MMDS revealed an intrusive $^{207}\text{Pb}/^{206}\text{Pb}$ age of 2.06 Ga (Mueller et al., 2004). Dike and sill emplacement in the region which occurred post-Tendoy orogeny and pre-Big Sky orogeny is evidence for regional extension with mafic dike emplacement at that time (Figure 23).

10.3. Post-extensional passive margin sedimentation and the 1.78-1.72 Ga Big Sky Orogeny

Following the Tendoy orogeny, synchronous with post 2.45 Ga rifting and dike emplacement, a second episode of sedimentation would have occurred on the continental margin at that time (Figure 23). This is supported by an abundance of marble sequences and other interlayered metasedimentary rocks which occur throughout the MMT. In the Ruby Range specifically, this is observed within the upper portion of the CRMS, which exhibits primarily ~1.78 Ga metamorphic ages indicating deposition post 2.45 Ga. However, it remains to be seen whether or not these sediments accumulated directly on the margin of the Wyoming craton or were part of an allochthonous terrane accreted onto the margin of the craton (Cramer, 2015). The accumulation of passive margin sediments is more likely, however, due to the prevalence of marbles with interlayered metapelitic lithologies.

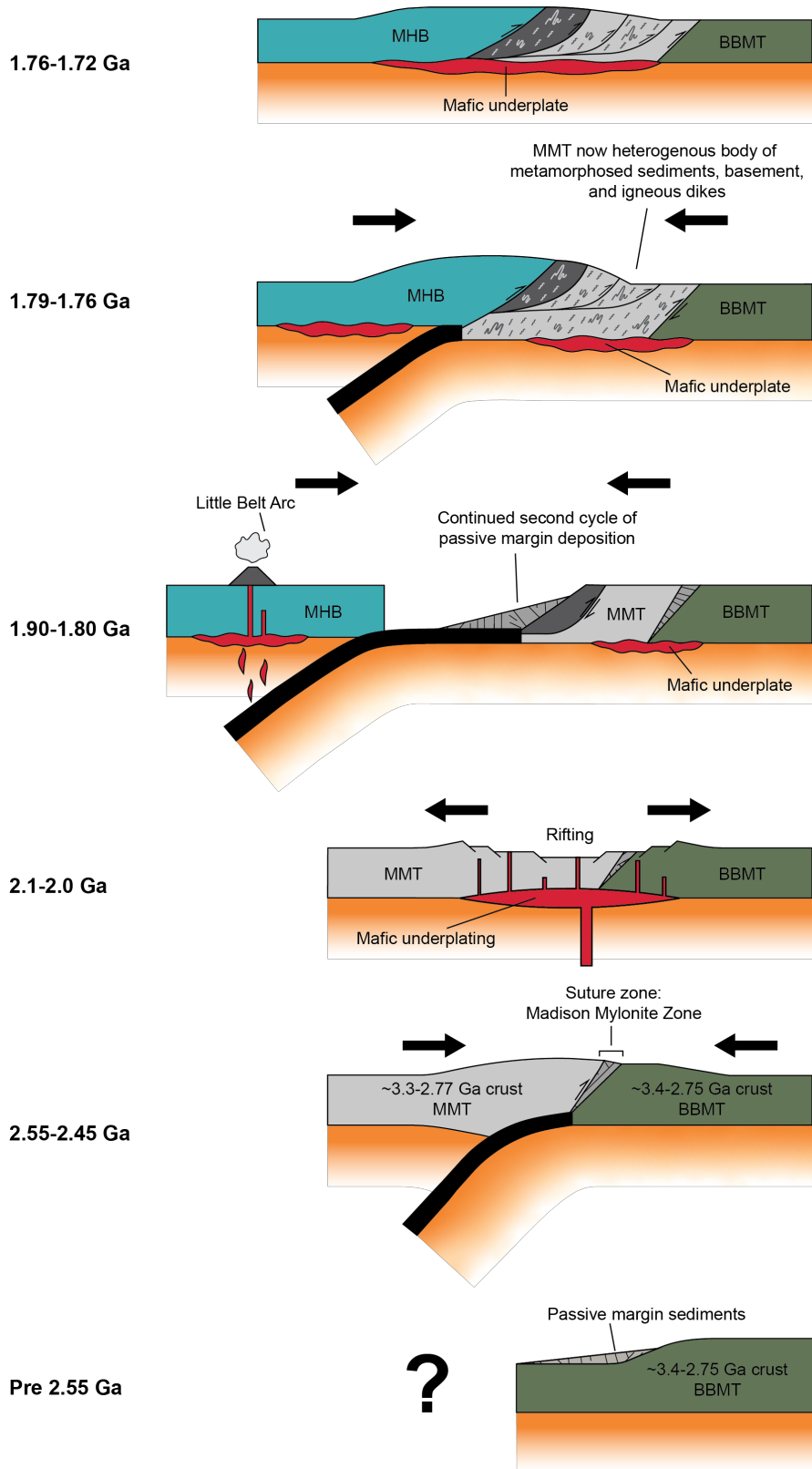


Figure 23. Schematic cross sections depicting the tectonic evolution of the NW margin of the Wyoming Province between ca 2.55-1.72 Ga. **Pre 2.55 Ga)** Accumulation of passive margin sediments. **2.55-2.45 Ga)** Tendoy orogeny – docking of MMT onto the crustal margin. **2.1-2.0 Ga)** Dike and sill emplacement associated with extensional tectonism. **1.90-1.80 Ga)** Onset of subduction of Wyoming Province beneath Medicine Hat Block and formation of Little Belt Arc. **1.79-1.76 Ga)** Big Sky orogeny: terminal collision between Wyoming Province and Medicine Hat Block. **1.76-1.72 Ga)** Formation of crustal architecture observed today.

As evidenced by previous geochronology from the Ruby Range and adjacent mountain ranges, the Wyoming Province collided with the Medicine Hat Block following ocean basin closure during the Paleoproterozoic Big Sky orogeny between 1.78-1.72 Ga (Figure 23). There are two basement exposures located within the GFTZ: the Little Rocky Mountains (LRM) and the Little Belt Mountains (LBM). Major element bulk geochemistry from a suite of calc-alkaline rocks in the LBM exhibit significant geochemical characteristics consistent with that of magma generated at a subduction zone (Mueller et al., 2002; Vogl et al., 2004). Similarly, geochemistry of orthogneisses from the LRM suggest the rocks either formed in a subduction zone environment, or represent remobilization of rocks that have an arc-signature (Gifford, 2013). The presence of a subduction zone is supported by Deep Probe geophysical data which exhibit dipping reflectors in the mantle just to the north of the GFTZ (Gorman et al., 2002; Vogl et al., 2004). New geophysical data from Gu et al. (2018) additionally support this interpretation after having observed significant crustal thickening and increased V_p/V_s ratios (ratio of compressional wave velocity to shear wave velocity) near the GFTZ, which favors the interpretation that the region represents a collisional orogen. Because the LBM and LRM are situated on the margin of the Medicine Hat Block, this would suggest northward directed subduction of the Wyoming Province beneath the Medicine Hat Block.

Cramer (2015) showed through monazite geochronology that crustal thickening and prograde metamorphism began ~ 1.79 Ga and culminated at ~ 1.76 Ga. This is likely when sediments from the second cycle of deposition were intercalated with Archean basement in addition to metasedimentary rock associated with the first cycle of deposition and the Tendoy orogeny. P - T modeling from this study show that the CRMS reached peak metamorphic conditions of ~ 7.7 kbar and ~ 760 °C and the EGS just off the western edge of the map area reached peak conditions of ~ 8 kbar and ~ 740 °C. This was followed by orogenic collapse between 1.76-1.71 Ga based on the replacement of garnet and sillimanite

by cordierite which was observed in both this study and Cramer (2015). Orogenic collapse during this time is also supported by increasing heavy rare earth element (HREE) abundance in monazite with decreasing age (Cramer, 2015).

11. Conclusions

P-T-t constraints suggest that each of the three major units within the Ruby Range have discrete metamorphic histories associated with the 1.78-1.72 Ga Big Sky orogeny. The CRMS consistently records peak pressures of ~ 7 kbar, however peak temperatures increase from ~700 °C at the top of the suite up to ~760 °C near the base. The Dillon Gneiss at the TOR locality records higher peak pressures, but similar peak temperatures as the base of the CRMS, yielding ~8.4 kbar and 760 °C. Peak *P-T* conditions from the EGS are less well constrained, and each locality discussed in this study yields discrete *P-T* results. The EGS locality situated in the southwestern corner of the Mine Gulch quadrangle reached peak conditions of ~6.8 kbar and ~735 °C, the locality immediately off the eastern edge of the quadrangle yielded conditions of ~7.7 kbar and 760 °C, the Elk Gulch locality yielded ~9 kbar and ~762 °C, and the Sweetwater Creek locality yielded ~8.6 kbar and ~778 °C. While variable, these results demonstrate that the EGS in the southern half of the Ruby Range preserves the highest peak metamorphic conditions not only out of all the EGS localities, but out of all three of the major structural units within the range.

New mapping interpretations and geochronology demonstrate that all three units within the Ruby Range are closely structurally and metamorphically intertwined. While the CRMS, DG, and EGS exhibit both ca. 2.45 Ga and ca. 1.78-1.72 Ga ages, the garnet leucogneiss and one sample from the lower CRMS contain exclusively 2.45 Ga ages. These new ages also aid in determining a refined metamorphic history for the western margin of the Wyoming Province between ca. 2.55-1.72 Ga. Prior to ~2.55 Ga,

sediment was accumulating on the cratonic margin. This was followed by collisional orogenesis involving the docking of the MMT to the Wyoming Province ca. 2.45 Ga, and a second cycle of sedimentation between ~2.45-1.8 Ga. Ca. 2.06 Ga, the region experienced dike and sill emplacement associated with extensional tectonism based on the age of mafic dikes identified in the Tobacco Root Mountains (Mueller et al., 2004). Then, between ~1.78-1.72 Ga, the Wyoming Province collided with the Medicine Hat Block to the north resulting the Big Sky orogeny. Collectively, the data discussed in this study aid in resolving the crustal architecture and thermotectonic history of the northwest margin of the Archean Wyoming Province throughout the Paleoproterozoic.

12. References

- Alcock, J., Muller, P.D., and Jercinovic, M.J., 2013, Monazite ages and pressure–temperature–time paths from anatexites in the southern Ruby Range, Montana, USA: evidence for delamination, ultramafic magmatism, and rapid uplift at ca. 1780 Ma: *Canadian Journal of Earth Sciences*, v. 50, p. 1069–1084.
- Baker, P.L., Vervoort, J.D., Baldwin, J.A., and Harms, T.A., 2017, Garnet Lu-Hf and zircon U-Pb dating constrains earliest Paleoproterozoic (2.43 Ga) thermal event in Ruby Range, SW Montana: *Abstracts with Programs - Geological Society of America*, v. 49.
- Caddick, M.J., Konopásek, J., and Thompson, A.B., 2010, Preservation of garnet growth zoning and the duration of prograde metamorphism: *Journal of Petrology*, v. 51, p. 2327–23479.
- Carlson, W.D., 2006, Rates of Fe, Mg, Mn, and Ca diffusion in garnet: *American Mineralogist*, v. 91, p. 1–11.
- Chamberlain, K.R., 1998, Medicine Bow orogeny: Timing of deformation and model of crustal structure produced during continent-arc collision, ca. 1.78 Ga, southeastern Wyoming: *Rocky Mountain Geology*, v. 33, p. 259–277.
- Chamberlain, K.R., Frost, C.D., and Frost, B.R., 2003, Early Archean to Mesoproterozoic evolution of the Wyoming Province: Archean origins to modern lithospheric architecture: *Canadian Journal of Earth Sciences*, v. 40, p. 1357–1374.
- Cheney, J.T., Webb, A.A.G., Coath, C.D., Mckeegan, K.D., and Webb, A.A.G., 2004, In situ ion microprobe 207 Pb / 206 Pb dating of monazite from Precambrian metamorphic suites, Tobacco Root Mountains, Montana: *Geological Society of America Special Papers*, v. 377, p. 151–179.
- Cramer, M., 2015, Proterozoic tectonometamorphic evolution of the Ruby Range, SW Montana, USA: Insights from phase equilibria modeling and in situ monazite petrochronology [M.S. Thesis]: The University of Montana, 120 p.
- Dahl, P.S., 1980, The thermal-compositional dependence of Fe²⁺-Mg distributions between coexisting garnet and pyroxene: applications to geothermometry: *American Mineralogist*, v. 65, p. 854–866.
- Dahl, P.S., Hamilton, M.A., Roberts, H.J., Kelley, S.P., Jercinovic, M.J., and Williams, M.L., 2002, Comparative ion and electron microprobe dating of Wyoming province monazite, with tectonic and analytical implications: *Abstracts with Programs - Geological Society of America*.
- Dahl, P.S., Hamilton, M.A., Wooden, J.L., Tracy, R.J., Loehn, C.W.I., Jones, C.L., and Foland, K.A., 2004, Do 2450–2480 Ma mineral ages from Wyoming cratonic margins (USA) indicate incipient breakup of supercontinent Kenorland: *Abstracts with Programs - Geological Society of America*, v. 36, p. 340.
- Dahl, P.S., Holm, D.K., Gardner, E.T., Hubacher, F.A., and Foland, K.A., 1999, New constraints on the timing of Early Proterozoic tectonism in the Black Hills (South Dakota), with implications for docking of the Wyoming province with Laurentia: *Bulletin of the Geological Society of America*, v. 111, p. 1335–1349.
- Desmarais, N.R., 1981, Metamorphosed Precambrian Ultramafic Rocks in the Ruby Range, Montana: *Precambrian Research*, v. 16, p. 67–101.
- Diener, J.F.A., and Powell, R., 2010, Influence of ferric iron on the stability of mineral assemblages: *Journal of Metamorphic Geology*, v. 28, p. 599–613.
- Erslev, E.A., and Sutter, J.F., 1990, Evidence for Proterozoic mylonitization in the northwestern Wyoming province: *Geological Society of America Bulletin*, v. 102, p. 1681–1694.
- Foster, D.A., Mueller, P.A., Mogk, D.W., Wooden, J.L., and Vogl, J.J., 2007, Proterozoic evolution of the western margin of the Wyoming craton: implications for the tectonic and magmatic evolution of

- the northern Rocky Mountains: *Canadian Journal of Earth Sciences*, v. 43, p. 1601–1619.
- Frost, C.D., Frueh, B.L., Chamberlain, K.R., and Frost, B.R., 2006, Archean crustal growth by lateral accretion of juvenile supracrustal belts in the south-central Wyoming Province: *Canadian Journal of Earth Sciences*, v. 43, p. 1533–1555.
- Gifford, J., 2013, *Precambrian Crustal Evolution in the Great Falls Tectonic Zone* [Ph.D. Thesis]: The University of Florida, 212 p.
- Gifford, J.N., Mueller, P.A., Foster, D.A., and Mogk, D.W., 2014, Precambrian Crustal Evolution in the Great Falls Tectonic Zone: Insights from Xenoliths from the Montana Alkali Province: *The Journal of Geology*, v. 122, p. 531–548.
- Giletti, B.J., 1966, Isotopic Ages from Southwestern Montana: *Journal of Geophysical Research*, v. 71, p. 4029–4036.
- Gorman, A.R., Clowes, R.M., Ellis, R.M., Henstock, T.J., Spence, G.D., Keller, G.R., Levander, A., Snelson, C.M., Buriannyk, M.J.A., Kanasewich, E.R., Asudeh, I., Hajnal, Z., and Miller, K.C., 2002, Deep Probe: imaging the roots of western North America: *Canadian Journal of Earth Sciences*, v. 39, p. 375–398.
- Hamelin, C., 2015, *Petrology, Geothermobarometry & Metamorphic History of Metapelites from the Central Ruby Range, Southwest Montana* [Undergraduate Thesis]: Smith College, 185 p.
- Harms, T.A., Brady, J.B., Burger, R.H., and Cheney, J.T., 2004, Advances in the geology of the Tobacco Root Mountains, Montana, and their implications for the history of the northern Wyoming province: *Geological Society of America Special Papers*, v. 377, p. 227–243.
- Harms, T.A., Burger, H.R., Blednick, D.G., Cooper, J.M., King, J.T., Owen, D.R., Lowell, J., Sincock, M.J., Kranenburg, S.R., Pufall, A., Picornell, C.M., Cooper, J.M., King, J.T., and Owen, D.R., 2004, Character and origin of Precambrian fabrics and structures in the Tobacco Root Mountains, Montana: *Geological Society of America Special Papers*, v. 377, p. 203–226.
- Heinrich, E.W., 1960, Geology of the Ruby Mountains, *in* Pre-Beltian geology of the Cherry Creek and Ruby Mountains areas, southwestern Montana, *Montana Bureau of Mines and Geology Memoir* 38, p. 15–40.
- Holland, T., and Powell, R., 2003, Activity-compositions relations for phases in petrological calculations: An asymmetric multicomponent formulation: *Contributions to Mineralogy and Petrology*, v. 145, p. 492–501.
- James, H.L., 1990a, *Geologic Map of the southwestern Ruby Range, Montana*: U.S. Geological Survey, scale 1:24,000.
- James, H.L., 1990b, *Precambrian Geology and Bedded Iron Deposits of the Southwestern Ruby Range, Montana*: U.S. Geological Survey Professional Paper 1495.
- James, H.L., and Hedge, C.E., 1980, Age of the basement rocks of southwest Montana: *Geological Society of America Bulletin*, v. 91, p. 11–15.
- Jones, C.L., 2008, U-Pb geochronology of monazite and zircon in Precambrian metamorphic rocks from the Ruby Range, SW Montana: Deciphering geological events that shaped the NW Wyoming province [M.S. Thesis]: Kent State University, 119 p.
- Kellogg, K.S., Snee, L.W., and Unruh, D.M., 2003, The Mesoproterozoic Beaverhead Impact Structure and Its Tectonic Setting, Montana-Idaho: $^{40}\text{Ar} / ^{39}\text{Ar}$ and U-Pb Isotopic Constraints: *The Journal of Geology*, v. 111, p. 639–652.
- Mogk, D.W., Mueller, P.A., and Wooden, J.L., 1992, The nature of Archean terrane boundaries: an example from the northern Wyoming Province: *Precambrian Research*, v. 55, p. 155–168.
- Mueller, P.A., Burger, H.R., Wooden, J.L., Brady, J.B., Cheney, J.T., Harms, T.A., Heatherington, A.L., and Mogk, D.W., 2005, Paleoproterozoic Metamorphism in the Northern Wyoming Province:

- Implications for the Assembly of Laurentia: *The Journal of Geology*, v. 113, p. 169–179.
- Mueller, P.A., Burger, R., Wooden, J.L., Heatherington, A.L., Mogk, D.W., and D'Arcy, K., 2004, Age and evolution of the Precambrian crust of the Tobacco Root Mountains, Montana: *Geological Society of America Special Papers*, p. 181–202.
- Mueller, P.A., and Frost, C.D., 2006, The Wyoming Province: a distinctive Archean craton in Laurentian North America: *Canadian Journal of Earth Sciences*, v. 43, p. 1391–1397.
- Mueller, P.A., Heatherington, A.L., Kelly, D.M., Wooden, J.L., and Mogk, D.W., 2002, Paleoproterozoic crust within the Great Falls tectonic zone: Implications for the assembly of southern Laurentia: *Geology*, v. 30, p. 127–130.
- Mueller, P., Mogk, D., and Wooden, J., 2012, Age and Composition of Crystalline Basement in the Armstead Anticline, Southwestern Montana: *Northwest Geology*, v. 41, p. 63–70.
- Mueller, P.A., Shuster, R.D., Wooden, J.L., Erslev, E.A., and Bowes, D.R., 1993, Age and composition of Archean crystalline rocks from the southern Madison Range, Montana: implications for crustal evolution in the Wyoming craton: *Geological Society of America Bulletin*, v. 105, p. 437–446.
- Mueller, P.A., Wooden, J.L., Nutman, A.P., and Mogk, D.W., 1998, Early Archean crust in the northern Wyoming province: Evidence from U-PB ages of detrital zircons: *Precambrian Research*, v. 91, p. 295–307.
- Pawley, M., Reid, A., Dutch, R., and Preiss, W., 2013, A user's guide to migmatites: Geological Survey of South Australia Report 2013-00016, 61 p.
- Powell, R., Holland, T., and Worley, B., 1998, Calculating phase diagrams involving solid solutions via non-linear equations, with examples using THERMOCALC: *Journal of Metamorphic Geology*, v. 16, p. 577–588.
- Roberts, H., Dahl, P., Kelley, S., and Frei, R., 2002a, New 207Pb – 206Pb and 40Ar – 39Ar ages from SW Montana, USA: constraints on the Proterozoic and Archæan tectonic and depositional history of the Wyoming Province: *Precambrian Research*, v. 117, p. 119–143.
- Roberts, H., Dahl, P., Kelley, S., and Frei, R., 2002b, New 207Pb-206Pb and 40Ar-39Ar ages from SW Montana, USA: Constraints on the Proterozoic and Archean tectonic and depositional history of the Wyoming province: *Precambrian Research*, v. 117, p. 119–143.
- Spear, F.S., Kohn, M.J., and Cheney, J.T., 1999, P -T paths from anatexis pelites: *Contributions to Mineralogy and Petrology*, v. 134, p. 17–32.
- Vogl, J.J., Foster, D.A., Mueller, P.A., Wooden, J.L., and Mogk, D.W., 2004, Lithology and age of pre-Belt Precambrian basement in the Little Belt Mountains, Montana: implications for the role of the Great Falls Tectonic Zone in the Paleoproterozoic assembly of North America: *Northwest Geology*, v. 33, p. 15–34.
- White, R.W., Powell, R., and Holland, T.J.B., 2007, Progress relating to calculation of partial melting equilibria for metapelites: *Journal of Metamorphic Geology*, v. 25, p. 511–527.
- White, R.W., Powell, R., Holland, T.J.B., Johnson, T.E., and Green, E.C.R., 2014, New mineral activity-composition relations for thermodynamic calculations in metapelitic systems: *Journal of Metamorphic Geology*, v. 32, p. 261–286.
- White, R.W., Powell, R., Holland, T.J.B., and Worley, B. a, 2000, The effect of TiO₂ and Fe₂O₃ on metapelitic assemblages at greenschist and amphibolite facies conditions: mineral equilibria calculations in the system K₂O-FeO-MgO-Al₂O₃-SiO₂-H₂O-TiO₂-Fe₂O₃: *Journal of Metamorphic Geology*, v. 18, p. 497–511.
- Whitmeyer, S.J., and Karlstrom, K.E., 2007, Tectonic model for the Proterozoic growth of North America: *Geosphere*, v. 3, p. 220.
- Wickham, S.M., 1987, The segregation and emplacement of granitic magmas: *Journal of the Geological*

Society, v. 144, p. 281–297.